Continuous Gravitational Waves from Galactic Neutron Stars: Demography, Detectability, and Prospects

Gianluca Pagliaro[1,2] , Maria Alessandra Papa[1,2] , Jing Ming[1,2] , Jianhui Lian[3,4] , Daichi Tsuna[5,6] ,
Claudia Maraston[7] , and Daniel Thomas[7]

[1] Max Planck Institute for Gravitational Physics (Albert Einstein Institute), Callinstraße 38, D-30167 Hannover, Germany; gianluca.pagliaro@aei.mpg.de,
maria.alessandra.papa@aei.mpg.de, jing.ming@aei.mpg.de
[2] Leibniz Universität Hannover, D-30167 Hannover, Germany
[3] Max Planck Institute for Astronomy, D-69117 Heidelberg, Germany
[4] Department of Physics & Astronomy, University of Utah, Salt Lake City, UT 84112, USA
[5] TAPIR, Mailcode 350-17, California Institute of Technology, Pasadena, CA 91125, USA
[6] Research Center for the Early Universe (RESCEU), School of Science, The University of Tokyo, 7-3-1 Hongo, Bunkyo-ku, Tokyo 113-0033, Japan
[7] Institute of Cosmology and Gravitation, University of Portsmouth, Dennis Sciama Building, Portsmouth, PO1 3FX, UK

Abstract

We study the prospects for the detection of continuous gravitational signals from normal Galactic neutron stars, i.e., nonrecycled stars. We use a synthetic population generated by evolving stellar remnants in time, according to several models. We consider the most recent constraints set by all-sky searches for continuous gravitational waves and use them for our detectability criteria. We discuss the detection prospects for the current and the next generation of gravitational-wave detectors. We find that neutron stars whose ellipticity is solely caused by magnetic deformations cannot produce any detectable signal, not even by third-generation detectors. The currently detectable sources all have $B \lesssim 10^{12}$ G and deformations that are not solely due to the magnetic field. For these, we find in fact that the larger the magnetic field, the higher the ellipticity required for the signal to be detectable, and this ellipticity is well above the value induced by the magnetic field. Third-generation detectors such as the Einstein Telescope and Cosmic Explorer will be able to detect up to ≈ 250 more sources than current detectors. We briefly treat the case of recycled neutron stars with a simplified model. We find that continuous gravitational waves from these objects will likely remain elusive to detection by current detectors, but should be detectable with the next generation of detectors.

1. Introduction

Continuous gravitational waves are expected to be emitted by neutron stars that present a degree of asymmetry with respect to their rotation axis. A number of mechanisms is thought to be responsible for these deviations from perfect axisymmetric configurations. Strongly magnetized neutron stars may present a deformation that is proportional to their magnetic field energy (Chandrasekhar & Fermi 1953; Ferraro 1954; Katz 1989; Haskell et al. 2008; Mastrano et al.2011) that in conjunction with a misalignment between the rotational and the magnetic field axis leads to nonaxisymmetry. Accreting objects may develop mountains due to nonaxisymmetric temperature variations in the crust (thermal mountains; Bildsten 1998; Ushomirsky et al. 2000) or to magnetic confinement of the accreted material (magnetic mountains; Brown & Bildsten 1998; Melatos & Payne 2005; Vigelius & Melatos 2009; Priymak et al. 2011). It has also been suggested that accreting neutron stars spinning rapidly enough to lead to crustal failure might eventually tend toward nonaxisymmetric equilibrium geometries (Giliberti & Cambiotti 2022).

The deformations can be accommodated by elastic crustal stresses (Ushomirsky et al. 2000; Haskell et al. 2006; Horowitz & Kadau 2009), or, for neutron stars with nonconventional matter composition, by elastic phases of matter in the deep core (Owen 2005; Haskell 2008). Regardless of the underlying mechanism, the neutron star asymmetry is typically described by the equatorial ellipticity $\varepsilon = |I_{xx} - I_{yy}|/I_{zz}$, where I_{ii} is the moment of inertia referred to as the i axis ($i = x, y, z$), and where z is aligned with the spin axis.

Continuous gravitational waves emitted by nonaxisymmetrically spinning neutron stars are nearly monochromatic signals that are practically on all the time. These signals are profoundly different from the gravitational-wave signals detected so far, which all come from compact binary coalescences—catastrophic events leading to major transformations of the emitting system, and lasting about some seconds. The amplitude of continuous waves is several orders of magnitude smaller than that of coalescence signals, and this major drawback is partly compensated for by the fact that they are long-lived. In principle, one can build up the signal-to-noise ratio by integrating the data over time. This unfortunately comes with huge computational costs.

The least computationally expensive continuous wave searches are the so-called targeted searches, where one targets a known object such as a pulsar, for which the sky-position and phase parameters (frequency and its time derivatives) are known from electromagnetic observations (Nieder et al. 2020; Ashok et al. 2021; Rajbhandari et al. 2021; Abbott et al. 2022a, 2022b, 2022c).

If the sky position of the object is known, but no information is available on the phase parameters, one can set up a directed

search and explore the free parameter space. This may be constrained by information on the object, such as its age (Zhang et al. 2021; Abbott et al. 2021b, 2022d; Ming et al. 2022; Owen et al. 2022). These searches are directed toward objects such as supernova remnants, low-mass X-ray binaries (LMXBs), or promising regions in the sky, and their computational cost is considerably higher than that of the searches for known pulsars.

At the top of the computational cost ladder are the all-sky surveys, where there are no specific targets, and the aim is instead to detect a signal from a previously unidentified object. In this case, assumptions on the expected signal population define the surveyed parameter space. Extensive searches are carried out (for a sample of recent results, see Dergachev & Papa 2021; Covas et al. 2022; Dergachev & Papa 2023; Abbott et al. 2021c, 2022e; Steltner et al. 2023), which have translated the no-detection results into constraints on the physical parameters of the subpopulation investigated so far.

Which fraction of the Galactic neutron star population is actually probed by the searches? Reed et al. (2021) found that while recent O2 data all-sky searches probe ellipticities below 10^{-6} for nearby objects, overall, they rule out ellipticities below 10^{-5} for only $\approx 1.6\%$ of all Galactic neutron stars.

The goal of this paper is to contribute to answering the question of the significance of the sample of objects probed by current searches by factoring in the astrophysical parameters relevant for the emission and the detection of continuous waves and their evolution time, and adding a detectability assessment to the discussion.

We use a population synthesis approach and generate a data set of $\approx 4.5 \times 10^8$ isolated nonaxisymmetric normal (nonre-cycled) neutron stars, starting from an initial distribution of neutron star progenitors, and dynamically evolving them throughout the Galaxy under the influence of the Galactic potential.

We consider different models that correspond to different combinations of the astrophysical priors that determine the spin evolution. We obtain various present-time populations, from which we study the characteristics of objects that are detectable by present and future detectors and their parameters.

This paper is organized as follows: in Section 2 we present the details of the synthetic population, and in Section 3 we describe the astrophysical priors that define the evolution models summarized in Section 3.3. In Sections 4 and 5 we present and discuss our results. Recycled neutron stars are treated in Section 6. We draw our conclusions in Section 7.

2. The Synthetic Neutron Star Population: Distribution in Space

Neutron stars are the stellar evolution remnants of massive stars. The lowest-mass star likely to generate a neutron star is around $8\,M_\odot$. Very high-mass stars are more likely to produce black holes than neutron stars, and the highest-mass star that still generates a neutron star depends on the specifics of the object evolution, such as its mass loss and rotation history. Indicatively, we take the highest-mass limit to be $40\,M_\odot$ (following Renzini & Ciotti 1993).

We generate a synthetic population of stars, identify those in the mass range $[8, 40]\,M_\odot$, and take them as the progenitors of neutron stars with mass $M = 1.4\,M_\odot$ (Renzini et al. 1993; Maraston 1998).
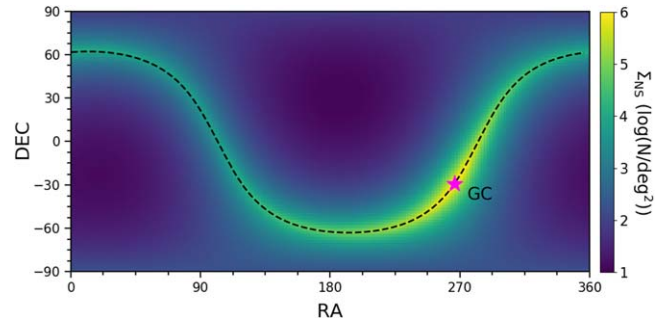

Figure 1. Surface density distribution of our synthetic neutron star population on the sky. The dashed black line indicates the Galactic plane, and the magenta star marks the Galactic center.

The stellar population is based on an initial stellar mass function (IMF), a simplified stellar spatial density model, and the formation rate history in the Milky Way.

For the IMF, we follow Kroupa (2001).

According to the stellar population models of Maraston (2005, 1998), for a Kroupa IMF, for instantaneous[8] stellar populations older than $\approx 30\,\mathrm{Myr}$ (i.e., the lifetime of an 8 solar mass star), we expect approximately 1% of the mass of all stars to be neutron stars. For simplicity, we assume the same mass fraction in neutron stars for populations of all ages older than $4\,\mathrm{Myr}$ (i.e., the lifetime of a $40\,M_\odot$ star, which is the mass threshold above which the remnant will be a black hole). In these calculations, the only (mild) dependence on metallicity is that of the turnoff mass and its lifetime (see Maraston 2005).

The density model focuses on the most massive stellar component of our Galaxy, the thin disk (Licquia et al. 2016), for which a standard exponential disk structure is assumed with a scale length of 2.6 kpc and a scale height of 0.3 kpc (Bland-Hawthorn & Gerhard 2016). We assume a spatially invariant star formation history (SFH) within the thin disk for simplicity, although a radially varying SFH is suggested in studies based on detailed stellar chemical abundances (e.g., Chiappini et al. 2001; Lian et al. 2020a, 2020b).

We assume an exponentially decreasing gas accretion history with an e-folding time of 10 Gyr, which is representative of the solar radius (Chiappini et al. 2001), and the Kennicutt-Schmidt star formation law (Kennicutt 1998). We set an initial gas accretion rate of $0.01\,M_\odot\,\mathrm{yr}^{-1}$. This results in a present-day stellar mass density of $0.050\,M_\odot\,\mathrm{pc}^{-3}$, which is close to observational results of 0.040–$0.043\,M_\odot\,\mathrm{pc}^{-3}$ in the solar neighborhood (Flynn et al. 2006; McKee et al. 2015; Bovy 2017). We also calculate the chemical enrichment history given the adopted gas accretion history using the chemical evolution model of Lian et al. (2018, 2020a).

By sampling the SFH, we obtain a synthetic catalog of neutron star progenitors that contains the 3D spatial position, age, and metallicity for $\sim 4.5 \times 10^8$ objects, which is broadly in line with other estimates in the literature (Diehl et al. 2006; Sartore et al. 2010).

Figure 1 shows the density distribution of neutron star progenitors in our synthetic catalog for all ages and distances on the sky. It is plotted in equatorial coordinates assuming an Earth position at 8.2 Kpc in Galactocentric radius and 27 pc above the disk plane (Bland-Hawthorn & Gerhard 2016). As expected, the overall density closely follows that of stars,

---

[8] Each star forms instantaneously, i.e., in a single burst.

peaking in the direction of the Galactic center, decreasing mildly in the anti-Galactic direction along the disk plane, and dropping dramatically when moving away from the disk plane. The age is independent of the sky position.

We associate with each neutron star progenitor a velocity based on disk stars observed today. This is obtained using 3D velocity measurement of ~300,000 disk stars in the APOGEE survey (Majewski et al. 2017) provided by the astroNN catalog (Mackereth & Bovy 2018; Leung & Bovy 2019), which are calculated using spectroscopic observations from APOGEE and astrometric observations from Gaia.

We evolve the position of each neutron star since birth using the procedures described in Tsuna et al. (2018). We account for the initial velocity of progenitors, natal kicks, and the Galactic gravitational potential.

Recent neutron star population synthesis studies (e.g., Vigna-Gómez et al. 2018) adopt two types of kicks depending on the supernova type. One is the conventional Maxwell distribution with $\sigma = 265$ km s^{-1} for core-collapse supernovae, and the other adopts $\sigma = 30$ km s^{-1} for electron-capture supernova. The kick velocity distribution we use is a combination of these two kick distributions. We assume a 75% core-collapse supernova population and a 25% electron-capture supernova population, reflecting the fact that this paper focuses on isolated neutron stars.

For each neutron star, we assign the kick velocity from the combined distribution, and we uniformly randomly assign a direction for that kick velocity. Combined with the initial velocity from its progenitor, the trajectory is evolved for the duration of its age. Thus, the velocity and spatial position of each neutron star at the present time is determined.

3. Spin-down Model and Astrophysical Priors

A magnetized nonaxisymmetric object looses rotational kinetic energy due to the emission of electromagnetic and gravitational waves. In the presence of an external dipolar magnetic field $B(t)$ and an equatorial ellipticity ε, the star's spin frequency ν evolves as

$$\dot{\nu} = -\frac{32\pi^3 R^6}{3Ic^3\mu_0}(B(t)\sin\chi)^2 \ \nu^3 - \frac{512\pi^4 GI}{5c^5}\varepsilon^2\nu^5. \quad (1)$$

We use this equation—valid in SI units and first introduced by Ostriker & Gunn (1969)—to evolve the spin of the star from birth to the present time.

In Equation (1), it is assumed that the spin axis coincides with one of the star's principal moments of inertia (no precession), and that the magnetic dipole moment is misaligned with respect to the rotation axis by an angle χ. R is the radius of the star, and I is the moment of inertia about the rotation axis. We fix the radius and the moment of inertia to the fiducial values $R = 12$ km and $I = 10^{38}$ kg m^2. For simplicity, we also assume $\sin\chi = 1$, thus considering every object to be an orthogonal rotator, also neglecting any spin-axis evolution in time. This, as shown by Bonazzola & Gourgoulhon (1996), implies that gravitational waves will be composed of a single harmonic at frequency $f_{GW} = 2\nu$.

In Section 3.1 we consider very broad models, encompassing the most common scenarios and parameter ranges. In this respect, these are partly agnostic models, but for ease of notation, we refer to them as agnostic models in the rest of the paper. In Section 3.2 we instead follow a specific empirical

model that is based on the works of Popov et al. (2010), Viganò et al. (2013), and Gullón et al. (2015).

3.1. Agnostic Models

These models are defined by a single distribution of neutron stars in the sky and a single magnetic field distribution, two distributions for birth spin frequencies, and two distributions for the ellipticity. Hence, all in all, we have four different A models. All the distributions are described below.

3.1.1. Magnetic Fields

Emission from isolated spinning neutron stars has been observed in the form of radio, X-ray, and γ-ray pulses, as well as nonpulsed radiation. The electromagnetic activity in neutron stars is intimately related to their magnetic field, whose magnitude can significantly vary depending on the neutron star type. Nonrecycled isolated neutron stars comprise radio-quiet central compact objects with inferred external magnetic fields of about $B = 10^{10-11}$ G, radio pulsars with $B = 10^{12-13}$ G, and magnetars with $B = 10^{14-15}$ G (Kaspi & Kramer 2016; Enoto et al. 2019). We hence consider a broad and agnostic distribution of magnetic field values,

$$p(\log_{10} B/[G]) = \mathcal{U}(10, 15), \quad (2)$$

where $\mathcal{U}(x_{\min}, x_{\max})$ indicates a uniform distribution between $x_{\min}$ and $x_{\max}$. We assume constant (time-independent) magnetic fields.

3.1.2. Ellipticity

The magnetic field of a neutron star causes deformations of its shape from perfect sphericity. Magnetic stresses are generated by the interaction between the conducting neutron star interior and the internal fields, producing deformations that scale linearly with the magnetic field energy. Assuming a mixed poloidal-toroidal geometry for the internal magnetic field, Mastrano et al. (2011) provide a relation that if rescaled to our fiducial value for the radius, assuming the mass of the neutron star to be $1.4\,M_\odot$, reads

$$\varepsilon(B, \Lambda) = 12.985 \times 10^{-6}\left(\frac{B}{5 \times 10^{14}\text{G}}\right)^2 \times \left(1 - \frac{0.385}{\Lambda}\right), \quad (3)$$

where Λ is the fraction of the magnetic energy stored in the poloidal component over the total magnetic energy of the star. In order to obtain it, the authors impose continuity at the surface of the star between the internal mixed field and an external dipole (e.g., the toroidal component vanishes at the surface). This is how the deformation is connected with the external magnetic field that drives the spin evolution. However, it must be understood that it is the internal field that causes the deformation, not the external one (Andersson 2020), and that unfortunately, there is no direct measurement of the former.

The range of variability for Λ is largely unknown. The consensus is that neither pure poloidal nor pure toroidal configurations are stable (Markey & Tayler 1973; Tayler 1973; Wright 1973; Braithwaite 2007; Kiuchi et al. 2008; Ciolfi et al. 2011; Lander & Jones 2011), but whether the magnetic field energy is dominated by one of the two components is a matter

of debate. In favor of configurations where the poloidal energy component is dominant, we point to the works by Ciolfi et al. (2010), Lander & Jones (2009), Lasky et al. (2012), and Lander et al. (2021), while Braithwaite (2009), Akgün et al. (2013) and Ciolfi & Rezzolla (2013) have argued in favor of a dominant toroidal component.

The last factor on the right-hand side of Equation (3) equals 0 when $\Lambda' = 0.385$, and it is positive (negative) if $\Lambda > \Lambda'$ ($\Lambda < \Lambda'$). A positive ellipticity means an oblate shape, while a negative ellipticity means a prolate shape.

We consider two scenarios.

Model 1: The magnetic field is the source of the deformation. For each synthetic object, with an assigned value for the external magnetic field B, we consider two values of Λ as follows:

    1. $\Lambda = 0.9$, consistent with Ciolfi et al., Lander et al., and roughly with Lander & Jones. We note that Lasky et al. (2012) find a stable configuration for $\Lambda = 0.65$. The resulting ellipticity is very close to that of the $\Lambda = 0.9$ configuration, however, making the two equivalent for the purpose of this study.

    2. $\Lambda = 0.1$, consistent with where results by Braithwaite, Akgün et al., and Ciolfi & Rezzolla overlap.

For each B and Λ, we take the ellipticity to be

$$\varepsilon = \min[\varepsilon(B, \Lambda), \varepsilon_{\max}], \tag{4}$$

with $\varepsilon(B, \Lambda)$ from Equation (3). Based on estimates of the maximum possible ellipticity sustainable by a neutron star (Ushomirsky et al. 2000; Haskell et al. 2006; Horowitz & Kadau 2009; Gittins et al. 2020; Gittins & Andersson 2021; Morales & Horowitz 2022), we set $\varepsilon_{\max} = 10^{-5}$.

Model 2: We do not specify the origin of the ellipticity, but we draw its value from a log-uniform distribution where the lower bound is due to the magnetic field. For each synthetic object, with an assigned value for the external magnetic field B, we draw the ellipticity from the following distribution:

$$p(\log \varepsilon) = \mathcal{U}(\log \varepsilon_{\min}, \log \varepsilon_{\max}) \tag{5}$$

and

$$\begin{cases} \varepsilon_{\min} = \varepsilon(B, \Lambda = 0.9) \\ \varepsilon_{\max} = 10^{-5}. \end{cases} \tag{6}$$

We choose $\Lambda = 0.9$ because it gives lower ellipticities with equal magnetic fields.

Two clarifications are needed. First, the ellipticity given originally by Mastrano et al. is not the equatorial ellipticity, but rather the oblateness. Since we are considering orthogonal rotators, these two coincide, and in the case of prolate objects, we simply take the absolute value of the ellipticity given by Equation (3). Second, we ignore the stability and secular evolution of oblate/prolate neutron stars with a fluid interior that exerts a centrifugal pressure on a solid crust. This pressure would tend to create a centrifugal bulge and thus a further change in shape (and likely in ellipticity) that might not be supported by the crust. Moreover, spinning oblate objects with a fluid interior are subject to a secular evolution different than prolate ones, with the former aligning their symmetry axis with the spin axis and the latter tending to orthogonal rotators configurations (Cutler & Jones 2000).

3.1.3. Birth Spin Frequency

The birth of a neutron star follows the hydrodynamical instability of the progenitor and its subsequent gravitational collapse(s). The remnant is more compact than the parent core, so the newborn neutron star possesses a much faster spin than the parent core. For a review of the topic, see Janka et al. (2001).

Theoretical efforts have been devoted to understanding the phenomenology of neutron star birth and the spin properties of newborn neutron stars (Heger et al. 2000, 2004, 2005; Ott et al. 2006; Camelio et al. 2016; Ma & Fuller 2019). Several authors have tried to extract information on the spin frequency at birth based on observational evidence (Faucher-Giguère & Kaspi 2006; Perna et al. 2008; Popov & Turolla 2012). In general, there is no consensus on the spin frequency distribution of newborn neutron stars.

A reasonable maximum spin frequency at birth is given by the Keplerian breakup limit, at which the spin is fast enough for the centrifugal force to overcome the star's own gravitational energy and breaks it apart. Haskell et al. (2018) estimate an equation-of-state-independent lower limit for the Keplerian breakup frequency at ≈1200 Hz. This value, however, applies only to matter and configurations of mature neutron stars. On the other hand, Camelio et al. (2016) show that the shedding-mass limit increases—and eventually saturates—during the first few tens of seconds after the core bounce. Applying this limit during this phase of the proto-neutron star leads to spin frequencies generally below 300 Hz. In this paper, we consider both estimates of the maximum birth spin frequency.

How slow can a neutron star spin at birth? The parameter that most affects the spin frequency at birth is the initial angular momentum of the post-bounce iron core (Ott et al. 2006; Camelio et al. 2016), which is largely unknown and poorly constrained.

Two main strategies exist to predict neutron star birth spin distributions; they resort to observational constraints. (i) Consider a set of pulsars with well-known phase parameters and evolve the spin frequency back in time to their birth (Popov & Turolla 2012). (ii) Consider a synthetic population of neutron stars such that when they are evolved to the present era, the observed spin distribution for pulsars is recovered (Faucher-Giguère & Kaspi 2006). In addition, Perna et al. (2008) propose a method based on the X-ray luminosities of a relatively large sample of supernovae to constrain the initial spin frequency of the newborn neutron star. In all the studies above, the slowest newborn neutron stars have spin periods of a few hundreds of milliseconds. In light of this, we set our lower bound to 2 Hz, which corresponds to a spin period of 500 ms.

We consider two log-uniform priors for the birth spin frequency:

    1. low: $p(\log \nu_0/[\mathrm{Hz}]) = \mathcal{U}(\log 2, \log 300)$
    2. high: $p(\log \nu_0/[\mathrm{Hz}]) = \mathcal{U}(\log 2, \log 1200)$.

Just as done above for the spin frequency ν, from here on we use the subscript 0 to refer to quantities at birth.

3.2. Empirical Models

Our empirical models, E models, are based on the studies of Popov et al. (2010), Viganò et al. (2013), and Gullón et al. (2015). These works assume electromagnetic spin-down only, and tune the magnetic field and birth spin frequency

distributions, in order to match the joint distributions of the observed population of magnetars, normal radio pulsars, and thermally emitting neutron stars. They also track the magnetic field decay through magnetothermal evolution codes. Here we consider models for the magnetic field and the birth spin frequency based on their results, as described below. For the ellipticity, we consider the distributions described in Section 3.1.2, but with the magnetic field values of this model.

Summarizing, the E models are defined by a single distribution of neutron stars in the sky and a single magnetic field distribution, two distributions for birth spin periods, and two distributions for the ellipticity. Hence, all in all, we have four different E models. All the distributions are described below.

3.2.1. Magnetic Field

For the distribution of magnetic fields at birth B_0, loosely following Gullón et al. (2015), we draw values from a truncated log-normal distribution,

$$p(\log_{10} B_0/[G]) = \begin{cases} \mathcal{N}(13, 0.8) & \text{if } B_0 \leqslant 10^{15}\,\text{G}, \\ 0 & \text{otherwise} \end{cases}, \quad (7)$$

with $\mathcal{N}(\mu, \sigma)$ indicating a normal distribution with mean μ and standard deviation σ.

In order to account for magnetic field decay, following Chattopadhyay et al. (2020) and Cieślar et al. (2020), we implement the following time dependence:

$$B(t) = (B_0 - B_{\min})e^{-t/\tau_B} + B_{\min}, \quad (8)$$

where τ_B is the decay timescale, and $B_{\min}$ is a lower limit for B. Equation (8) essentially describes a field that decays exponentially when $t \lesssim \tau_B$ and then saturates to values on the same order as $B_{\min}$ for $t > \text{few} \cdot \tau_B$. This implementation wants to mimic what found in magnetothermal simulations where the magnetic field decays significantly in the first 10^5–10^6 yr to then slow down, and from a few million years after birth, remains almost constant (Popov et al. 2010). We hence choose $\tau_B = 10^6$ yr and set $B_{\min}$ to the value taken by the magnetic field at $t = 10 \cdot \tau_B$ as if the decay were purely exponential (i.e., $B_{\min} = B_0 \cdot e^{-10}$).

3.2.2. Birth Spin Frequency

The authors of the studies mentioned at the beginning of this section all reason in terms of spin period rather than spin frequency. We thus draw spin periods P_0 for the newborn neutron stars of our synthetic population, and then transform these into spin frequencies through the relation $\nu_0 = \frac{1}{P_0}$. We consider two models:

1. norm: $p(P_0/[\text{ms}]) = \mathcal{N}(300, 200)$. This is consistent with Popov et al. (2010), Viganò et al. (2013), and Gullón et al. (2015).
2. unif: $p(P_0/[\text{ms}]) = \mathcal{U}(0.8, 500)$. This is justified by the fact that Gullón et al. (2015) argue that the overall population statistics is not very sensitive to the initial spin distribution, and find that by slightly readjusting the rest of the parameters, any nearly uniform distribution in the range $0 < P_0/[\text{ms}] < 500$ reproduces the present-day spin distribution just as well. To some extent, the same conclusion is drawn by Gonthier et al. (2004), who

consider the radio-pulsar population only, and by Gullón et al. (2014), who additionally consider X-ray thermally emitting pulsars. The minimum value of $0.8\,\text{ms} = 1250\,\text{Hz}$ roughly corresponds to the Keplerian breakup frequency mentioned in Section 3.1.3.

3.3. Model Summary

In total, we have eight models: four are the agnostic A models of Section 3.1, and the other four are the empirical E models of Section 3.2. The four combinations come from two models for ε, 1 and 2,[9] and two models for f_0 or P_0, high/low and unit/norm for A and E, respectively. All in all, we therefore have A1$_{\text{low}}$, A1$_{\text{high}}$, A2$_{\text{low}}$, A2$_{\text{high}}$, E1$_{\text{unif}}$, E1$_{\text{norm}}$, E2$_{\text{unif}}$, and E2$_{\text{norm}}$. A summary of the model parameters is given in Table 1.

4. Spin Evolution

Every newborn neutron star has a position, age, and an initial velocity; as described in Section 2, its position is evolved in time, yielding a present-day position. The present-time $\nu - \dot{\nu}$ distribution is determined by values drawn from the different distributions of B_0 (or B in the case of static magnetic fields), ε, and ν_0, depending on the model, and Equation (1). We thus obtain a distinct population of neutron stars for each model adopted.

We integrate the spin-down Equation (1) by approximating the spin evolution to be solely determined by magneto-dipole emission—in limiting cases—because then the present-time spin frequency is attainable analytically (see, e.g., section II of Wade et al. 2012). In particular, setting $\sin \chi = 1$, we can rewrite the spin-down Equation (1) as

$$\begin{cases} \dot{\nu} = \gamma_{\text{dip}} \nu^3 + \gamma_{\text{GW}} \nu^5 \\ \gamma_{\text{dip}} = -\dfrac{32\pi^3 R^6}{3Ic^3\mu_0}B^2, \quad \gamma_{\text{GW}} = -\dfrac{512\pi^4 GI}{5c^5}\varepsilon^2. \end{cases} \quad (9)$$

In the case of a stationary magnetic field (models A), the spin-down is approximately purely magneto-dipolar if

$$\frac{\gamma_{\text{GW}}\nu^5}{\gamma_{\text{dip}}\nu^3} < \frac{1}{100} \Rightarrow \gamma := \frac{\gamma_{\text{GW}}}{\gamma_{\text{dip}}} < \frac{10^{-2}}{\nu^2}. \quad (10)$$

Since the RHS of Equation (10) is minimized at higher frequencies, we choose our condition for pure magneto-dipole spin-down to be

$$\gamma < 10^{-8}\,s^2, \quad (11)$$

which is what we obtain from Equation (10) if we set $\nu = 1000\,\text{Hz}$, which is close to the highest frequency of our models.

For the models with magnetic field decay (models E), the condition for pure magneto-dipolar emission has to be satisfied at the present time (lowest B). The analytical relation that gives the present-time spin frequency in this case is given by Chattopadhyay et al. (2020) in Equation (6) of their work.

The gravitational-wave-dominated spin-down limit cannot occur for models A, while it is extremely improbable and in

---

[9] Model 1 ellipticity models consider both values of Λ, as explained in Section 3.1.2. For each such model, every realization is performed twice, once for revery value of Λ.

Table 1
Models Summary

Model Name	Magnetic Field (G)	Birth Spin Frequency (Hz)	Ellipticity
A1$_{low}$	log-uniform: $10^{10} \leqslant B \leqslant 10^{15}$	log-uniform: $2 \leqslant \nu_0 \leqslant 300$	Model 1
A1$_{high}$	"	log-uniform: $2 \leqslant \nu_0 \leqslant 1200$	"
A2$_{low}$	"	log-uniform: $2 \leqslant \nu_0 \leqslant 300$	Model 2
A2$_{high}$	"	log-uniform: $2 \leqslant \nu_0 \leqslant 1200$	"
E1$_{norm}$	log-normal:[a] $\mu_{\log_{10} B_0} = 13$, $\sigma_{\log_{10} B_0} = 0.8$	See Section 3.2	Model 1
E1$_{unif}$	"	See Section 3.2	"
E2$_{norm}$	"	See Section 3.2	Model 2
E2$_{unif}$	"	See Section 3.2	"

Notes. The ditto mark means "same as above".
[a] Cutoff at 10^{15} G.

practice never realized for models E because it requires ellipticities $\approx 10^{-5}$ and magnetic fields about 5 sigma away from their mean value.

In the γ ranges outside of Equation (11), we integrate numerically following different procedures based on the model considered. These are explained in detail in Appendix A.

For each model, we perform 100 realizations of the synthetic population. The frequency evolution of each object is calculated on the ATLAS cluster at AEI Hannover.

Table 2 shows the number of sources whose gravitational-wave frequency—rotation frequency $\times$ 2—lies in the band of ground-based gravitational-wave detectors. We see that less than 1% of the population of the considered neutron stars falls in the band of the current detectors, but if the lower frequency is pushed down by only 15 Hz, the number of sources increases twentyfold. A band starting at 5 Hz is plausible for the next generation of gravitational-wave detectors.

The nearest neutron star is found at a distance of 11 ± 3 pc on average, which is consistent with what can be estimated based on general arguments (see, e.g., Dergachev & Papa 2020), but it increases to 94 ± 35 pc when we consider neutron stars spinning in-band alone.

5. Detectability

With the present-time spin frequency at our disposal, we can evaluate both the instantaneous intrinsic spin-down through Equation (1) and the dimensionless strain amplitude h_0 resulting from each synthetic neutron star,

$$h_0 = \frac{4\pi^2 G I}{c^4 d} f_{GW}^2 \varepsilon, \qquad (12)$$

where d is the neutron star's distance from Earth.

We consider the following three recent all-sky searches:

1. Dergachev & Papa (2021, 2023) based on Advanced LIGO O2 and O3 data, respectively (sometimes referred to as the Falcon searches).
2. Abbott et al. (2022e) based on Advanced LIGO and Advanced Virgo O3 data.[10]
3. Steltner et al. (2023) based on Advanced LIGO O3 data.

A neutron star is considered to be detectable by a certain search if its gravitational-wave signal frequency and frequency derivative fall within the parameter space covered by that

---

[10] We consider all pipelines except for the SOAP pipeline, which is the least sensitive.

Table 2
Number of Sources in-band and Relative Percentage with Respect to the Galactic Neutron Star Population for Current ($N_{f_{GW} > 20Hz}$) and Future Detectors ($N_{f_{GW} > 5Hz}$) Computed as the Average Over the 100 Realizations Performed

Model	$N_{f_{GW} > 20Hz}$	$N_{f_{GW} > 5Hz}$
A1$_{low}$	$4.9 \times 10^5 (0.14\%)$	$9.9 \times 10^6 (2.9\%)$
A1$_{high}$	$5.6 \times 10^5 (0.16\%)$	$10.2 \times 10^6 (3\%)$
A2$_{low}$	$4.8 \times 10^5 (0.14\%)$	$9.9 \times 10^6 (2.9\%)$
A2$_{high}$	$5.5 \times 10^5 (0.16\%)$	$10.2 \times 10^6 (3\%)$
E1$_{norm}$	$7.4 \times 10^5 (0.22\%)$	$23.2 \times 10^6 (6.9\%)$
E1$_{unif}$	$1.6 \times 10^6 (0.47\%)$	$29.1 \times 10^6 (8.7\%)$
E2$_{norm}$	$6.7 \times 10^5 (0.20\%)$	$23.1 \times 10^6 (6.9\%)$
E2$_{unif}$	$1.4 \times 10^6 (0.43\%)$	$29.1 \times 10^6 (8.7\%)$

Notes. For models 1 we show only the results for $\Lambda = 0.1$. The results for $\Lambda = 0.9$ are very similar. During the course of its life, a neutron star may drift outside of the Galaxy—with a kick velocity of 300 km s^{-1}, a 10^{10} yr old neutron star can drift by 300 kpc. Out of the $\approx 4.5 \times 10^8$ in the initial population, we now find $N \approx 3.5 \times 10^8$ within 50 kpc of the Galactic center, which is a generous estimate of the horizon distance for continuous waves in this frequency range for the next decade of observations. This is what we consider as our population.

Table 3
Expected Number of Currently Detectable Neutron Stars, Computed as the Average $\pm 1\sigma$ Over the 100 Realizations Performed

Model	$\bar{n}$	% of in-band
A2$_{low}$	1.4 ± 1.16	0.0003
A2$_{high}$	3.62 ± 1.91	0.0007
E2$_{norm}$	0.01 ± 0.1	$\approx 10^{-6}$
E2$_{unif}$	0.01 ± 0.1	$\approx 10^{-6}$
A1	<0.01	...
E1	<0.01	...

Note. The last column shows the percentage probed with respect to the total number of sources in-band for each model (second column of Table 2). The remaining models, here indicated generally as A1 and E1, give no detectable signal in any of the realizations.

search, and if it has an amplitude h_0 greater than or equal to the upper limit set by the search at that frequency. We say that an object is currently detectable if it is detectable by at least one of the searches considered above.

Table 3 shows that the percentage of in-band sources that give rise to signals that could be currently detectable is very low. With such a small number of detectable signals, it is hard to extract a reliable expected value for the closest detectable
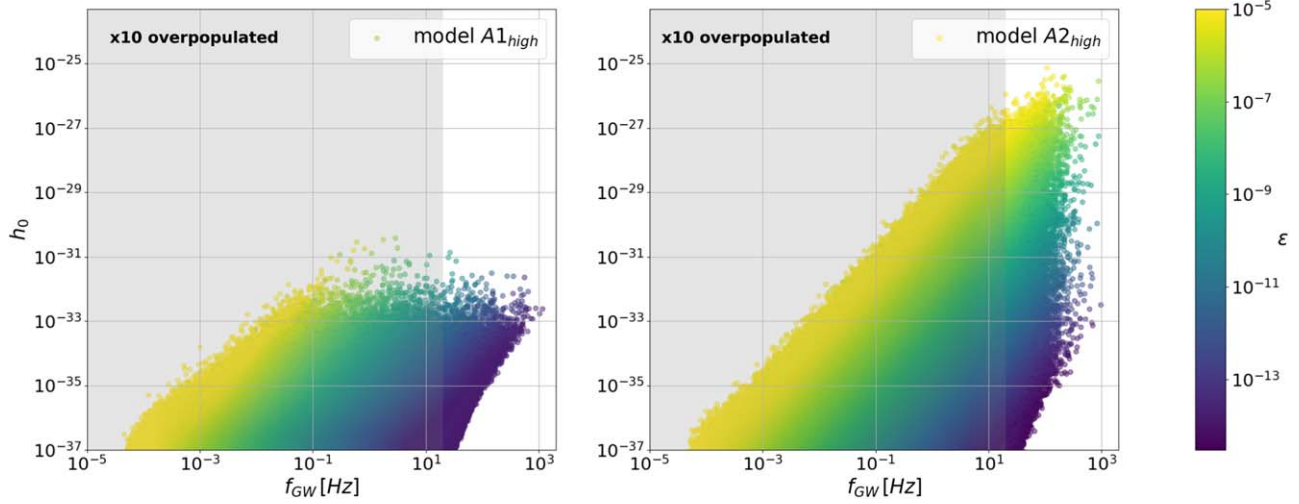
Figure 2. $f_{GW} - h_0$ of the neutron star populations. The color encodes the ellipticity. The shaded region indicates out-of-band frequencies. In models A1, the ellipticity only stems from the magnetic field. In models A2, the population is endowed with ellipticities drawn from a log-uniform distribution. We see that the highest-ellipticity objects in model A1 spin out of the band that is useful for detection, and those that remain in the useful band can do so because they have a weak magnetic field and hence a low ellipticity. Conversely, in model A2, the ellipticity is not solely dependent on the magnetic field, and hence we have low magnetic field objects that remain in-band that are endowed with a high ellipticity.

star. For model A2$_\text{high}$—the model with the highest statistics—we compute the average distance of the closest and of the farthest detectable neutron star. We find $d_\text{close} = 1.05 \pm 1.08$ kpc and $d_\text{far} = 5.71 \pm 3.01$ kpc, with 70% of the closest neutron stars detectable within 1.5 kpc of Earth.

5.1. Magnetically Deformed Neutron Stars

We first consider models A1 and E1, where the ellipticity stems from the magnetic field alone. We find that they cannot produce signals that are detectable by current or by future detectors considered in Section 5.3, regardless of the value of Λ. In fact, the strongest signals from these models have amplitudes of about 10^{-29}–10^{-28}, which is three to four orders of magnitude smaller than current upper limits and more than 50 times smaller than the estimated sensitivity to continuous gravitational waves of third-generation detectors (this can be seen in the summary figure, Figure 11, at the end of the paper).

The reason why the strongest signals from these models are still very weak is that sources with a high value of ellipticity must have a very high magnetic field, and consequently, a very fast spin-down that quickly pulls them to very low frequencies and out of the instrument bands. Additionally, because $h_0 \propto f_\text{GW}^2$, a lower frequency means a quadratically smaller h_0 (see Equation (12)), so as the star spins down, the amplitude of the gravitational wave decreases. The only objects whose frequency remains high are those with weak magnetic fields and hence are the tenuously deformed ones (see Figure 2).

5.2. Currently Detectable Sources

Among all our models, only those where the ellipticity is drawn as outlined by model 2 (Section 3.1.2) currently give detectable objects, but just barely and with large uncertainties. Table 3 summarizes the results. We study agnostic models first.

Considering model A2$_\text{high}$, which is the most populated by currently detectable sources, we look at the plot of Figure 3. This shows how the average number $\bar{n}_\text{bin}(B, \varepsilon)$ of currently detectable sources depends on the magnetic field B and on the

ellipticity ε; these two quantities are binned in log scale in 10 intervals in both dimensions. When $\bar{n}_\text{bin}(B, \varepsilon) < 1$, it can be interpreted as the probability of finding a detectable source with a magnetic field and an ellipticity that are within the ranges spanned by that bin. We find that the constant $\bar{n}_\text{bin}$ curves (dashed gray lines in the plot) are well described by straight lines of the form

$$\log_{10} \varepsilon = a \log_{10} B/[G] + b(\bar{n}_\text{bin}), \tag{13}$$

where $a \approx 1$, and b depends on the isoprobability value $\bar{n}_\text{bin}(B, \varepsilon)$.

We can invert Equation (13) and find a functional form for $\bar{n}_\text{bin}(B, \varepsilon)$. In order to do so, we study how b depends on $\bar{n}_\text{bin}$ and find $b(\bar{n}_\text{bin})$ to be well approximated by a quadratic polynomial, that is, monotonic in the range of values shown in the color bar of Figure 3. We hence substitute the quadratic $b(\bar{n}_\text{bin})$ in Equation (13), solve for $\bar{n}_\text{bin}$ as a function of B and ε, and find

$$\bar{n}_\text{bin}(B, \varepsilon) = 0.245(1 - \sqrt{g(B, \varepsilon)}), \tag{14}$$

where

$$g(B, \varepsilon) = 0.56 \left(a \log_{10} B/[G] - \log_{10} \varepsilon\right) - 8.39. \tag{15}$$

We stress that Equation (14) was empirically derived based on the results shown in Figure 3, so its validity outside of that (B, ε) range has not been verified. Furthermore, it is not valid in the white region of Figure 3, corresponding to $\bar{n}_\text{bin} < 0.001$, for which it yields negative values. On average, in its range of validity, the relative difference between our fit and the original results is 65%.

We now turn to a qualitative explanation of why the constant detection-probability lines in the (ε, B) are of the form $\varepsilon \propto B$.

From Equation (1), setting $\sin \chi = 1$, we find that the time it takes a neutron star that is born with an initial spin frequency ν_0 to spin down to a frequency ν as a function of its ellipticity and
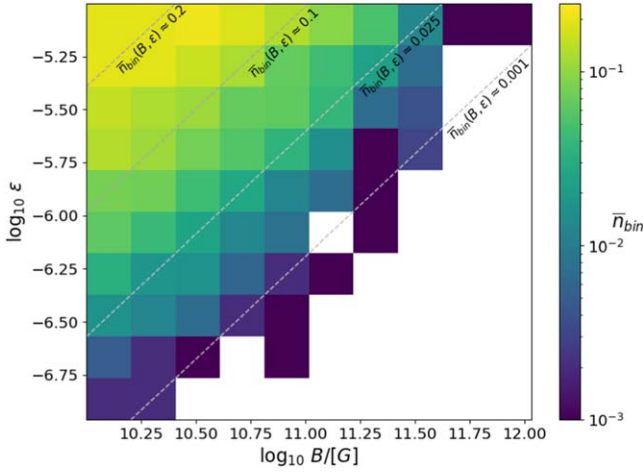
Figure 3. 2D histogram showing $\bar{n}_{bin}(B, \varepsilon)$ color-coded for model A2$_{high}$. In order to increase the resolution, we considered a higher number of realizations: 1000. The white bins are bins without detected sources, hence $\bar{n}_{bin} < 10^{-3}$.

magnetic field is

$$\tau(\nu; \nu_0, \varepsilon, B) = \frac{1}{2|\gamma_{dip}|}\left[\frac{\nu_0^2 - \nu^2}{\nu_0^2 \nu^2} + \gamma \ln\left(\frac{\nu^2}{\nu_0^2}\left(\frac{1 + \gamma\nu_0^2}{1 + \gamma\nu^2}\right)\right)\right],$$

(16)

where from Equations (9) and (10), we recall that $\gamma_{dip} \propto B^2$ and $\gamma \propto \frac{\varepsilon^2}{B^2}$.

Figure 4 shows $\tau(B)$ for $\nu = 10$ Hz and $\nu_0 = 500$ Hz as a function of B for various values of the ellipticity ε. For high values of B, the second term in the right-hand side of the equation above is negligible, and $\log \tau \propto -\log B$ (i.e., the plot is a straight line with a slope of -1). Only for $B \lesssim 10^{10}$ G and $\varepsilon \gtrsim 10^{-6}$ does the loss of energy through gravitational waves due to the ellipticity become resolvable, with clearly longer evolutions for lower ellipticities.

Our agnostic models all have $B \geqslant 10^{10}$ G, where the spin-down evolution is mostly dominated by the magnetic field. In this regime, if $\nu_0 \gg \nu$, then τ is largely independent of ν_0, and we can take the curves of Figure 4 to be representative of the spin-down time for a signal to reach 10 Hz, starting from a sufficiently high birth spin frequency (indicatively above 100 Hz). This says that all sources older than

$$\tau^{age} \approx \frac{1}{2|\gamma_{dip}|\nu_{min}^2} = 5.4 \times 10^8 \text{ yr}\left(\frac{10^{10} \text{ G}}{B}\right)^2\left(\frac{10 \text{ Hz}}{\nu_{min}}\right)^2$$

(17)

are rotating slower than ν_{min}.

How many stars are younger than τ^{age}? Because we assume a constant birthrate of $\mathcal{R} \approx 4 \times 10^{-2}$ yr^{-1}, the number of stars younger than τ^{age} is simply the number of objects born between now and a time τ^{age} in the past,

$$N(\tau^{age}) = \mathcal{R} \cdot \tau^{age} \approx 2.16 \times 10^7\left(\frac{10^{10} \text{ G}}{B}\right)^2\left(\frac{10 \text{ Hz}}{\nu_{min}}\right)^2.$$

(18)

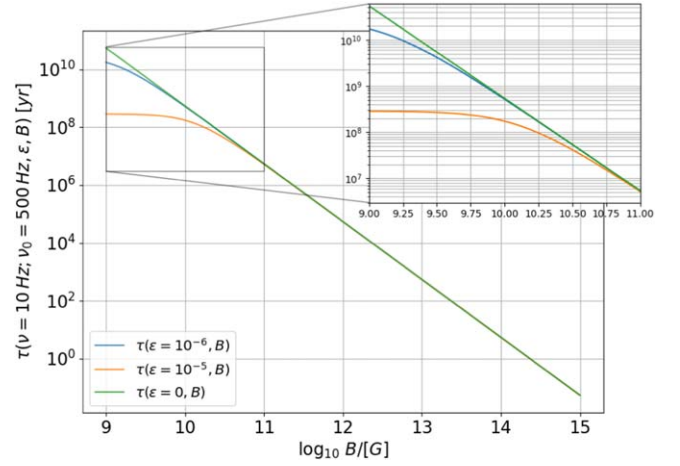This is also approximately the number of objects spinning faster than ν_{min}.

Figure 4. Spin-down time τ as from Equation (16) as a function of the magnetic field.

From Equation (18), we see that if B increases, the number of objects spinning faster than ν_{min} decreases $\propto B^{-2}$. On the other hand, the total number of objects within a given distance $N(d)$ is approximately proportional to d^2 (this proportionality is exact if the neutron stars are distributed on a plane), and out of these, only those above some h_0 value will be detectable. So with increasing B, the overall number of objects in-band decreases, but the number of detectable ones could be kept constant by increasing $\varepsilon \propto d$ according to Equation (12). Therefore, the lines of the constant number of detectable sources have a slope of ≈ 1 in the $\log B - \log \varepsilon$ plane, with the low B/high ε combination being the most favorable for detection, as was also found by Wade et al. (2012).

5.2.1. Impact of the Birth Spin Frequency

The comparison of the results from models A2$_{low}$ and A2$_{high}$ tells us something about the impact of the birth spin frequency on the detectability. The difference between the two models is that the highest birth spin frequency in the low model is 300 Hz, whereas in the high model, it is 1200 Hz. Because the birth spin frequencies are distributed log-uniformly, only $\approx 22\%$ of the neutron stars in A2$_{high}$ have $\nu_0 \in [300$ Hz, 1200 Hz$]$, but they account for $\approx 66\%$ of the detectable sources. This means that under the astrophysical assumptions outlined by our A models, the probability of a neutron star born with a spin frequency above 300 Hz to emit a currently detectable signal is about seven times higher than that of a neutron star born with a spin frequency below 300 Hz. We explain the last statement explicitly in Appendix B.

5.2.2. Phase Parameters and Sky Distribution

Figure 5 shows how the phase parameter space region covered by the different searches compares to the region occupied by the strongest signals (the definition of a strong signal is given in the caption of the figure). The latter is overall well covered by ongoing efforts. There is a very scarcely populated region in this plot that is routinely searched, but that might be dropped in principle based on our results: the high $\dot{f}$ region at frequencies $\lesssim 130$ Hz. Because this is a relatively small region compared to the bulk of parameter space typically investigated and the computational cost scales at least with the square of the frequency, however, the overall benefit gained by
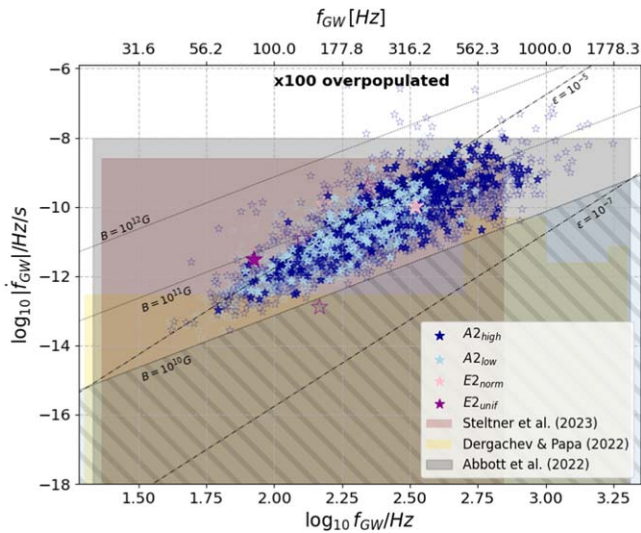
Figure 5. f_{GW}–$\dot{f}_{GW}$ distribution of strong signals, that is, signals that are currently detectable (filled opaque stars) or are within a factor of 3 of being detectable (empty transparent stars). The colored areas correspond to the parameter space portions that are covered by the all-sky searches mentioned in Section 5. For the few sources that fall outside of the $f - \dot{f}$ region covered, the amplitude is compared to the upper limit set by the FrequencyHough pipeline in Abbott et al. (2022e) at the frequency closest to the signal frequency. The $(f_{GW}, \dot{f}_{GW})$ of putative sources evolving due to purely electromagnetic emission are shown by the dotted lines, and those due to gravitational braking by the dash–dotted lines. The strong sources in the white areas—i.e., not covered by any search— amount to less than 0.5% of all sources in the plot. E2 signals are marked with a larger and thicker star. The hatched area is ignored in models A because we set $B_{\min} = 10^{10}$ G in these models.

excluding the region at issue would not result in a significant saving of resources. It is hence unlikely that the savings coming from becoming completely blind to signals from this region could be fruitfully reinvested to significantly increase the sensitivity of the searches in other regions of the parameter space.

Table 4 shows the expected number of detectable objects in various frequency ranges, having taken model $A2_{high}$ as our reference model, as done before. The table also shows how the expected number of detectable signals changes as the detector sensitivity increases. There are a number of competing factors that determine the detectability in different bands. Namely, the frequency dependence on the detector noise, the likelihood of having a source in any band, and the proportionality between the amplitude of a signal and the square of its frequency. The detector sensitivity curve favors the medium band, the signal occupancy favors the low band, and the frequency dependence of the signal amplitude favors the high band.

Our results suggest that the medium-frequency band lies on a sweet spot and is the major contributor to the overall detectability. Furthermore, at the current sensitivity, the high band contributes significantly more than the low band. However, as both Table 4 and Figure 6 show, this trend slowly reverses as the detector sensitivity increases, and it is definitely inverted at sensitivities 10 times higher than the current one, i.e., the level expected for next generation of ground-based detectors. This effect is clearly amplified for detectors—such as the Einstein Telescope (ET)—that promise a significantly improved performance at low frequencies.

The smallest band that currently contains 90% of the detectable signals is the band at [65, 545] Hz, with this interval shrinking and shifting to the left to [45, 380] Hz in the case of
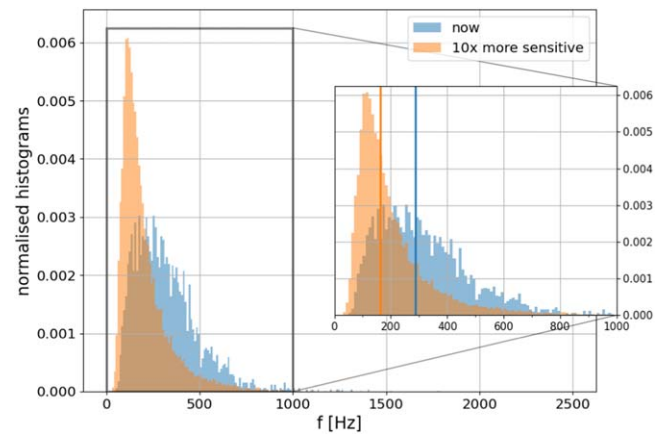

Figure 6. Distribution of the frequency of signals from model $A2_{high}$ that are detectable now and with higher (tenfold) sensitivity detectors/searches. The vertical solid lines located at 162 and 287 Hz indicate the median of the same-color histogram.
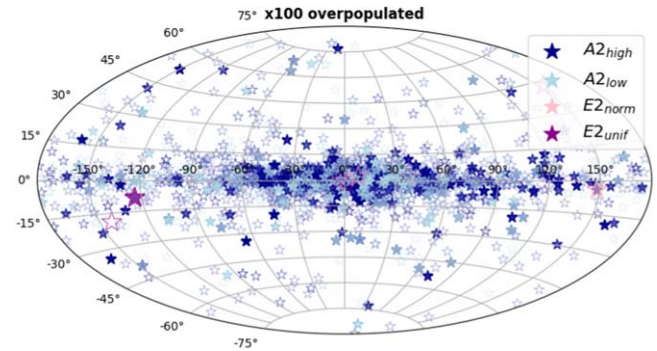

Figure 7. Distribution on the sky (Galactic coordinates) of signals that are detectable (filled opaque stars) and that are within a factor of 3 of being detectable (empty transparent stars), as in Figure 5.

Table 4
Average Number of Detectable Objects per Frequency Band for Model $A2_{high}$

Low [20, 100] Hz	Medium [100, 500] Hz	High [500, 2400] Hz
	Now	
0.12	3.08	0.42
	$2\times$ more sensitive	
0.69	11.26	1.37
	$3\times$ more sensitive	
1.79	23.23	2.5
	$10\times$ more sensitive	
33.77	170.12	9.74

detectors/searches that are 10 times more sensitive than current ones.

All strong signals shown in Figure 5 are also plotted in the sky map of Figure 7. We consider the region within 15° the Galactic plane. It contains ≈81% of all strong signals of model $A2_{low}$ and ≈86% of all strong signals of model $A2_{high}$ (we ignore signals from $E2_{norm}$ and $E2_{unif}$ because of their small statistical sample size). These percentages are significantly higher than the percentage of objects within the same region from the entire synthetic neutron star population, that is, 63.5%. This is due to the fact that strong signals come by and large

from young sources, and because most neutron stars are born within a narrow region of the Galactic plane, the young ones have not had enough time to migrate away from it.

To return to the fact that depending on the model, ≈81%–86% of all strong signals lie within 15° of the Galactic plane, a similar percentage (about 85%) is found within the same sky region in the ATNF catalog (Manchester et al. 2005) if pulsars in globular clusters as well as recycled ones are discarded. Since—similarly to the gravitational-wave case—also EM detections from isolated nonrecycled pulsars are subject to selection bias toward young objects, this last fact can be considered a consistency check of our synthetic population.

5.2.3. Models E2

To conclude this section, we briefly comment on the results from models E2.

For both $E2_{norm}$ and $E2_{unif}$, only one signal out of the 100 realizations was found to be detectable. This might appear surprising given that the E-model populations have more stars in-band than the A-model ones (see Table 2). The reason for this is as follows. Assuming that the contribution of the ellipticity to the spin evolution is negligible and assuming a constant magnetic field, Equation (17) says that the time it takes a system to spin down to a frequency ν from a much higher starting frequency is proportional to $1/B^2$. Hence, if the magnetic field is not constant but decays, it takes a longer time for the star to spin down to ν. This occurs if the spin-evolution timescale (based on the initial magnetic field) is longer than the magnetic field decay timescale τ_B because in this case, the magnetic field decays appreciably during the spin-evolution. So when

$$5.4 \times 10^8 \, \text{yr} \left(\frac{10^{10} \, \text{G}}{B_0} \right)^2 \left(\frac{10 \text{Hz}}{\nu_{min}} \right)^2 > \tau_B \Rightarrow$$

$$\Rightarrow B_0 \leqslant 2.3 \times 10^{11} \, \text{G} \left[\frac{10 \, \text{Hz}}{\nu_{min}} \right], \tag{19}$$

the star will stay in-band indefinitely.[11] A star like this will not be detectable, however, because ellipticities generally higher than 10^{-6} are necessary for a detection today, and objects with high ellipticities like this would have spun down to frequencies below 10 Hz; see the zoomed inset of Figure 4. We recall that under the assumption of a constant birthrate, 99% of the neutron stars today are at least 10^8 yr old.

However, as the sensitivities of both searches and detectors improve, the chances to be able to detect a less deformed object increase. Indeed, the strongest signals of models E2 are not too far below the current upper limits, and, as we discuss in the next section, these models become interesting for third-generation detectors (see also the summary figure, Figure 10, at the end of the paper).

5.3. Third-generation Detectors

We now wish to investigate the prospects of a detection by the third-generation ground-based gravitational-wave detectors the ET (Punturo et al. 2010; Maggiore et al. 2020) and Cosmic Explorer (CE; Dwyer et al. 2015). For the ET, we use the

Table 5
Average Number of Sources Detectable by the ET and CE with Searches Comparable with the Advanced LIGO Data Searches (Abbott et al. 2022e; Steltner et al. 2023)

Model	$\bar{n}$		% of in-band
	ET	CE	
$A2_{low}$	231.9 ± 14.6	338.1 ± 16.8	0.003%
$A2_{high}$	387.2 ± 19.4	524.3 ± 22.6	0.005%
$E2_{norm}$	0.5 ± 0.6	2.0 ± 1.4	0.00001%
$E2_{unif}$	1.7 ± 1.3	5.2 ± 2.2	0.00002%

Note. The last column is obtained considering the total detectable sources by either the ET or CE, and similarly to Table 3, represents the fraction of detectable sources over the total number of sources in-band for each model (third column of Table 2).

sensitivity estimates presented in Hild et al. (2011), labeled there "ET-D" in the equilateral triangle configuration, while for the CE, we use the single-detector 40 km baseline configuration as defined in Srivastava et al. (2022).

In order to assess the detectability of a population of signals using the estimated sensitivity of the proposed detectors, we proceed as follows. As a measure of the sensitivity of a search, we take the upper-limit values, and from those, we define the sensitivity depth (Behnke et al. 2015),

$$\mathcal{D}^C \equiv \frac{\sqrt{S_h(f)}}{h_0^C(f)} \, [1/\sqrt{\text{Hz}}], \tag{20}$$

where $h_0^C(f)$ are the amplitude upper limits at confidence level C, and $S_h(f)$ is the spectral density of the noise. The sensitivity depth is a property of the search, and it measures how deep a certain search method could dig into a given detector noise.

Assuming that the same search on ET and CE data would be performed as was performed on LIGO data, we estimate the expected upper limits simply by solving Equation (20) for $h_0^{95\%}$ by using the predicted third-generation detectors $S_h(f)$ and the sensitivity depth $\mathcal{D}^{95\%}$ of the LIGO data search,

$$h_0(f)^{95\%} = \frac{\sqrt{S_h(f)}}{\mathcal{D}^{95\%}} \sqrt{\frac{2}{N}}, \tag{21}$$

where N is the number of third-generation detectors equivalent to the number of detectors used in the LIGO data search. The three-arm design of the ET is equivalent to a system of three advanced-generation detectors (Hild et al. 2011), so $N^{ET} = 3$, whereas we conservatively take $N^{CE} = 1$.[12]

We can now compare the predicted upper limits from Equation (21) with our synthetic signal population and determine how many are detectable. We simplify the detectability criteria such that any signal whose amplitude is larger than or equal to the upper limit at the frequency of the signal is considered to be detectable, regardless of the rest of the signal parameters. Of the signals that are detectable according to this criterion, ≈99% have $|\dot{f}| < 10^{-8}$ Hz s^{-1} (so within the currently searched range), so this simplification does not introduce any significant bias.

---

[11] In fact, for E models, we have ≈10^7 objects with $B_0 < 2.3 \times 10^{11}$ G, which is consistent with the ≈10^6 in-band objects from Table 2, considering that not all spins at birth are very high.

[12] The main 40 km CE observatory might be combined with a 20 km detector. In this case, however, we cannot simply consider $N^{CE} = 2$ because Equation (21) is valid only when the various detectors are of comparable sensitivity.

Table 6
Average Number of Detectable Objects per Frequency Band in Different Models for the CE

Model	Low [5, 100] Hz	Mid [100, 500] Hz	High [500, 2500] Hz
$A2_{low}$	151.59	186.73	0.53
$A2_{high}$	193.2	318.02	15.15
$E2_{norm}$	1.83	0.21	0.0
$E2_{unif}$	4.38	0.78	0.02

The results are summarized in Table 5. For a more detailed picture, we refer to the summary Figures 10 and 11 at the end of the paper. If the ellipticity is purely generated by the magnetic field as per models A1 and E1, not even the third-generation gravitational-wave detectors are likely to see a signal. Conversely, all of our models in which the ellipticity is log-uniformly distributed up to a maximum value of 10^{-5} (Model 2 defined in Section 3.1.2) give detectable signals.

Table 6 shows the average number of sources that are detectable by third-generation detectors in three different frequency ranges, and it highlights the importance of a better low-frequency sensitivity. Compared to the ranges defined in Section 5.2.2, the low-frequency band is now pushed down to 5 Hz and the high band is pushed up to 2500 Hz. The chances of a detection of a signal from population model $A2_{high}$ in the low band grows by a factor ≈ 1000 with respect to current detectors.

The magnetic field decay introduced in model E2 has a large impact on the number of sources detectable by third-generation detectors, enhancing the chances of detection, as shown in Figure 8. The magnetic field decay makes it possible for old sources (up to several billion years) that are born with fields $B \lesssim 10^{11.5}$ G to still be in-band (Equation (19)). This creates an additional population of detectable signals with respect to the static magnetic field population, which appears as the high-age concentration blob in Figure 9. However, as already explained in Section 5.2.3, these very old in-band sources cannot be maximally deformed ($\varepsilon \lesssim 3 \times 10^{-6}$).

6. Recycled Neutron Stars

In the past sections, we have considered the frequency evolution of populations of normal neutron stars from birth until now and obtained synthetic present-day populations. We have seen that a major factor impacting the detectability of stars in these populations is their frequency, i.e., whether they have spun during their evolution down to frequencies too low to be detectable.

From electromagnetic observations of pulsars, we know that there exists another category of neutron stars—so-called recycled objects—rotating faster than the typical normal neutron star, which makes them very interesting for continuous gravitational-wave detection.

A recycled neutron star is an old neutron star that has been spun up to spin periods of about milliseconds as a result of total angular momentum conservation during an accretion phase (Alpar et al. 1982; Radhakrishnan & Srinivasan 1982; Bhattacharya & van den Heuvel 1991). An example of such objects are millisecond pulsars (MSPs), which are visible in the electromagnetic spectrum as radio, X-ray, and gamma sources. For a review of MSPs, see Lorimer (2008).

Like for the spatial distribution of MSPs, the distribution of Galactic recycled neutron stars might be quite different than that of normal ones. Moreover, the evolutionary path that links
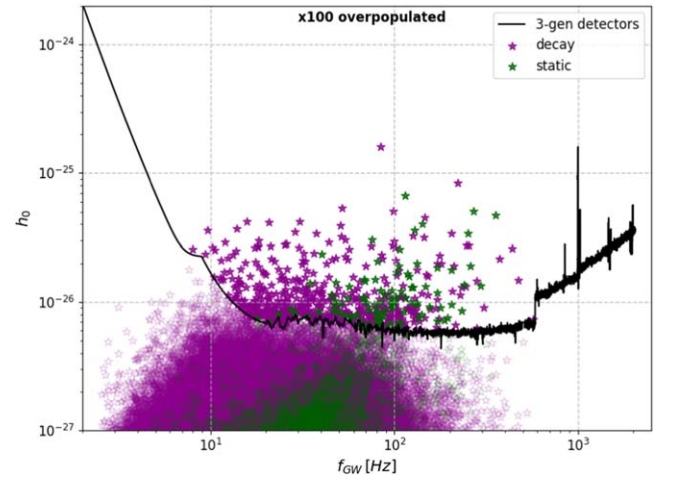

Figure 8. The gravitational-wave amplitude of signals (stars) and the expected third-generation detector sensitivity. Magenta stars represent signals from model $E2_{unif}$, which includes magnetic field decay, but for this comparison, we show the signals from the same model, but with a static magnetic field (dark green stars).
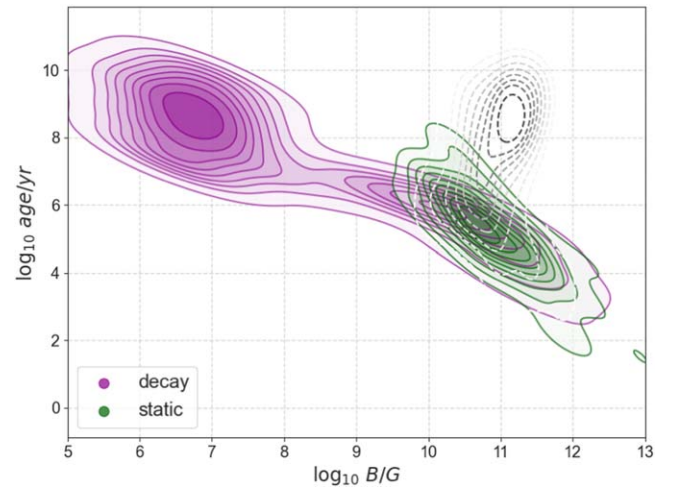

Figure 9. Kernel density estimation plot of the number density of third-generation detectable sources as a function of magnetic field and age for the two populations shown in Figure 8. The dashed empty contours (in black and white) represent the magenta population objects at birth. The contour levels reach from 0 to 100% in steps of 10%.

a recycled neutron star with its progenitor binary star system is complex, with the outcome of the recycling generally coupled with the binary parameters. Modeling this mechanism is beyond the scope of this paper. Because this population is so relevant for continuous waves, however, here we consider a simplified population of nonaccreting fully recycled neutron stars (Tauris 2011) and use it to make a first detectability assessment and compare with the results for the population of normal neutron stars.

For the spatial distribution, we opt for a simple snapshot approach. Assuming the Galactic population of recycled neutron stars to follow that of MSPs, we consider the spatial distribution that Grégoire & Knödlseder (2013) adopt in their work, which is in turn based on the results of Story et al. (2007),

$$p(\rho, z) \propto \exp(-\rho/\rho_0)\exp(-|z|/z_0), \qquad (22)$$

where $\rho_0 = 4.2$ kpc and $z_0 = 0.5$ kpc are the radial and vertical scale heights, respectively. In Equation (22) we use cylindrical
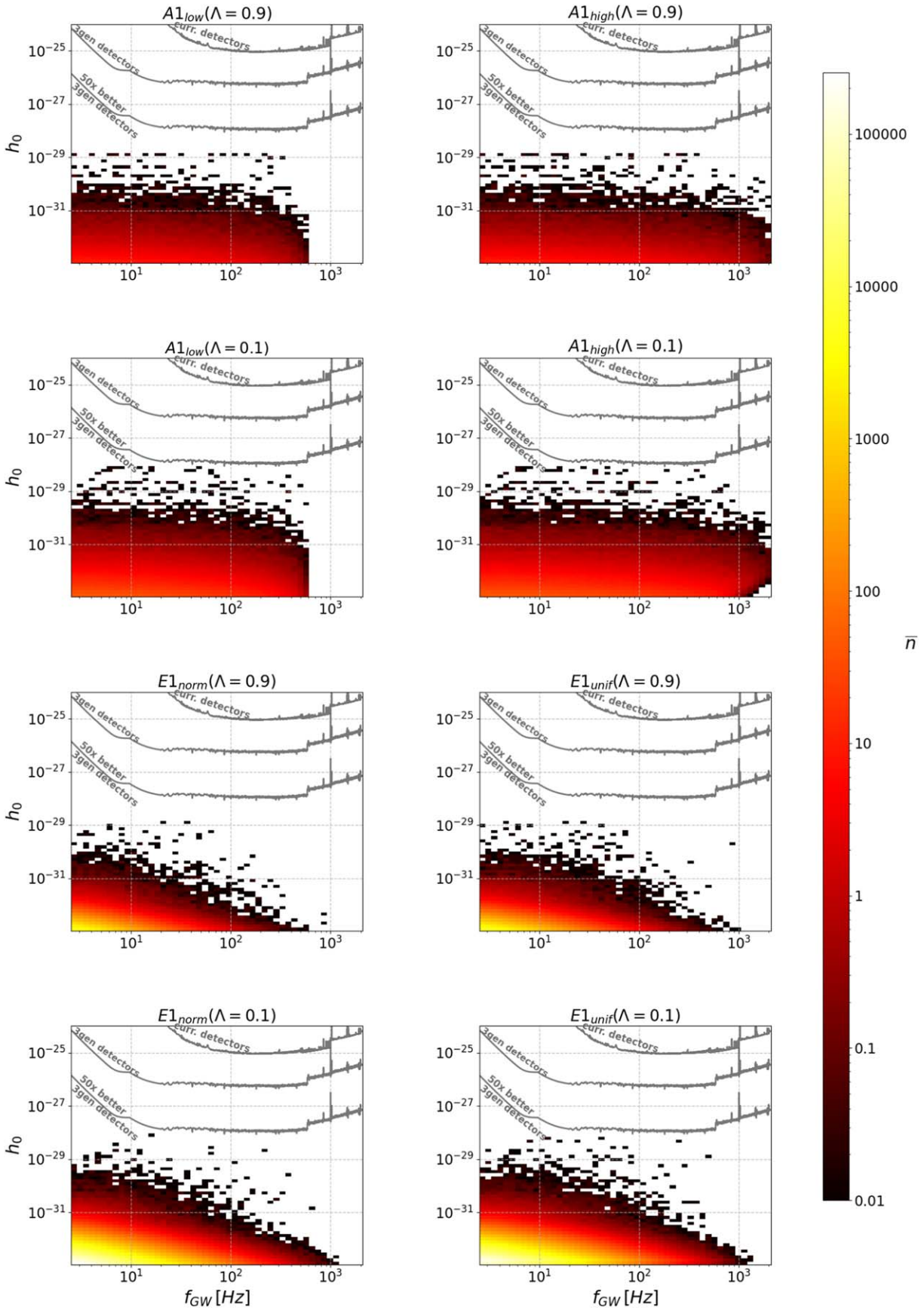
Figure 10. Normal neutron stars: 2D histograms showing the expected number of sources at each $f_{GW} - h_0$ bin, $\bar{n}$. There are 50 log-uniform bins in frequency and h_0. The frequency interval is [2 Hz–2100 Hz], and the h_0 interval is [10^{-34}–10^{-27}]. The curve for current detectors is based on published searches for isolated neutron stars. The "3gen detectors" line is a sensitivity projection based on forecast noise curves and assumes search methods as sensitive as current searches. At each frequency, we use the best sensitivity between the ET and the CE detectors, as explained in Section 5.3. The "50x better 3gen detectors" line is the "3gen detectors" line divided it by 50.
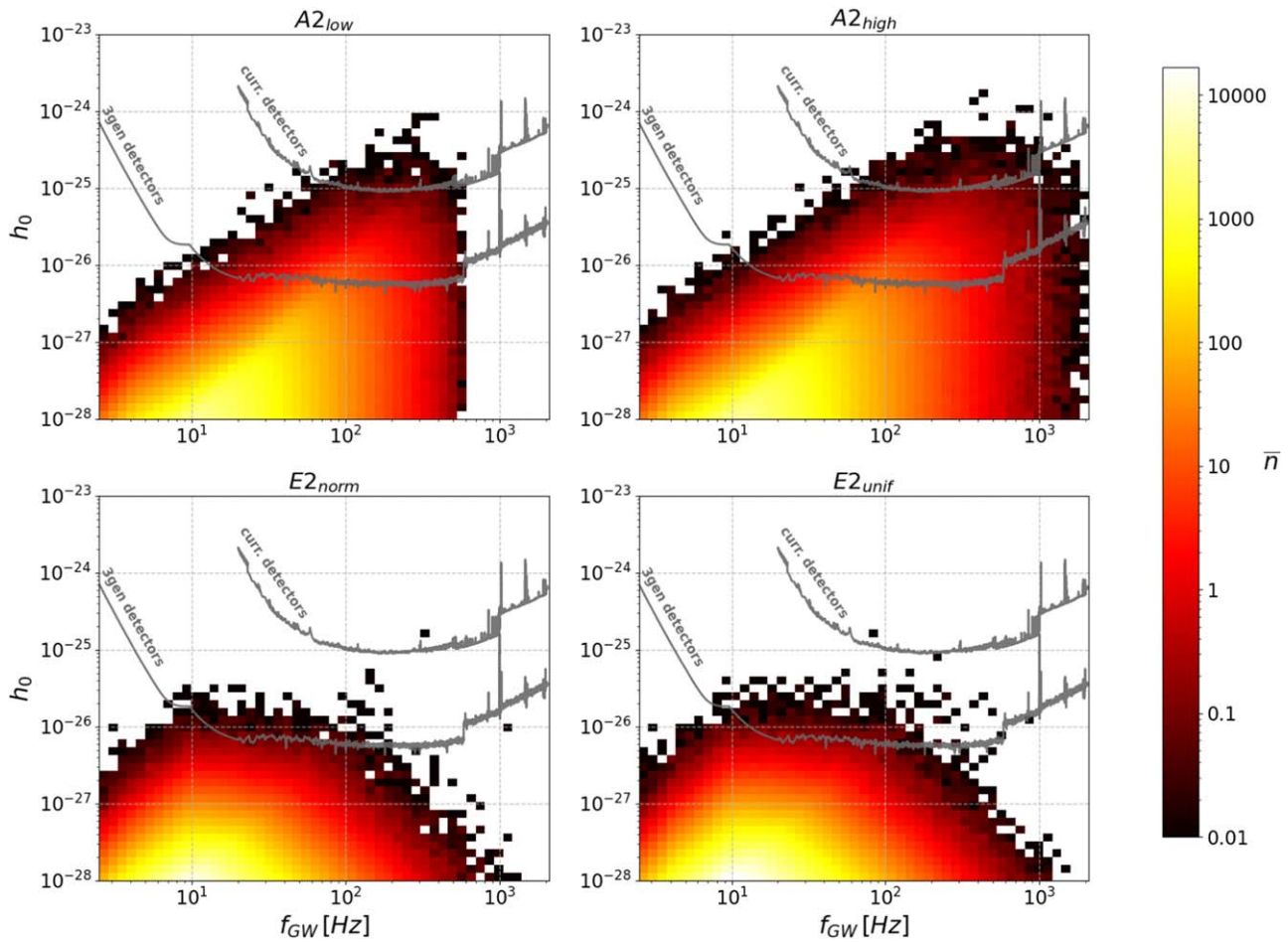
Figure 11. Same as Figure 10, but for models for which the ellipticity is drawn from a log-uniform distribution, as explained in Section 3.1.2 for Model 2. There are 50 log-uniform bins in frequency and h_0. The frequency interval is [2 Hz–2100 Hz], and the h_0 interval is [10^{-28}–10^{-23}].

coordinates whose origin is coincident with the center of the galaxy. ρ is the radial coordinate, while z is the axial coordinate. Azimuthal isotropy is assumed, so the azimuth coordinate is uniformly distributed within 0 and 2π.

We assume a constant birthrate of 5×10^{-6} yr^{-1} in the last 12 Gyr[13], resulting in a population of $N^{\mathrm{MSP}} = 60{,}000$ objects. The birthrate is obtained by Story et al. from the total number of MSPs in the disk and is consistent with the detected population, and it agrees loosely with those obtained by Ferrario & Wickramasinghe (2007) and Grégoire & Knödlseder (2013, extended sample case).

Magnetic fields are drawn from a log-uniform distribution between 10^7 and 10^9 G (Manchester et al. 2005).

For the ellipticity, we adopt the same models as described in Section 3.1.2, but because the external magnetic field values in recycled systems are not high enough to give a significant deformation through Equation (3), we consider only Model 2 of Section 3.1.2.

We let every object be recycled to the same initial spin frequency of 700 Hz, which roughly corresponds to the observed cutoff frequency value in accreting millisecond X-ray pulsars (Chakrabarty 2008), and evolve it through Equation (1). We find a much higher fraction of objects in-band compared to normal

neutron stars: $N_{f>20\mathrm{Hz}}/N^{\mathrm{MSP}} = 0.96$ and $N_{f>5\mathrm{Hz}}/N^{\mathrm{MSP}} = 1$ for recycled objects versus less than 1% and 10% for the 20 Hz and 5 Hz cutoff, respectively, for normal neutron stars (see Table 2). This is consistent with the much lower magnetic fields assumed for recycled neutron stars. These higher fractions of in-band objects will not translate into a higher detection probability for recycled systems because there are far fewer objects overall.

Fully recycled neutron stars are observed in binary systems and as isolated objects. For this reason, we also consider in addition to the searches for signals from isolated objects of Section 5 the following upper limits from all-sky searches for neutron stars in binaries to establish detectability:

1. Covas & Sintes (2020) based on Advanced LIGO O2 data.
2. Abbott et al. (2021a) based on Advanced LIGO O3a data.
3. Covas et al. (2022) based on Advanced LIGO O3a data.

The per-Hz cost of these searches is considerably higher than for all-sky searches for signals from isolated objects because the parameter space includes at least the three binary parameters of the orbital period, the projected semimajor axis, and the time of ascending nodes. Because one operates within a limited computing budget, this results in a lower sensitivity. We have not considered Singh & Papa (2023), who searched orbital parameters that are unlikely to pertain to recycled neutron stars.

---

[13] By "birth" we mean the birth of a recycled neutron star, i.e., immediately after the end of the recycling process.

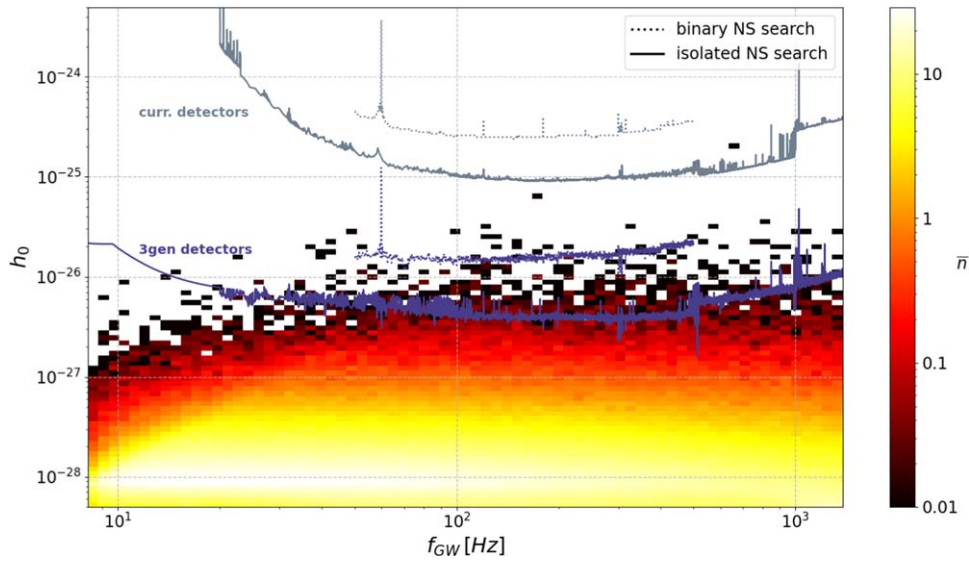**Figure 12.** Recycled systems: 2D histograms showing the expected number of sources at each $f_{GW} - h_0$ bin, $\bar{n}$. There are 100 log-uniform bins in frequency and h_0. The frequency interval is [2 Hz–2100 Hz], and the h_0 interval is [5×10^{-29}–5×10^{-24}]. The solid curves for current detectors refer to published searches for isolated neutron stars, and the dotted curves refer to published searches for neutron stars in binary systems. The "3gen detectors" lines are sensitivity projections based on the forecast noise curves and assume search methods as sensitive as the current ones. At each frequency, we use the best sensitivity between the ET and CE, as explained in Section 5.3.

Table 7
Average Number of Detectable Sources $\bar{n}$ under Different Assumptions on the Proportions of the Number of Binary-to-isolated Neutron Stars

	(All Binary)	$\bar{n}$ (All Isolated)	(Mix)
now	<0.01	0.01 ± 0.1	<0.01
CE	0.18 ± 0.38	5.8 ± 2.62	3.44
ET	0.09 ± 0.29	4.76 ± 2.32	2.8

Note. In the mix model, we have assumed 42% isolated objects and 58% in binaries, consistent with the ATNF MSP population. We recall that the total population is 60,000 objects.

We determine the detectability of isolated neutron stars and neutron stars in binaries separately. We count as detectable any isolated signal whose amplitude lies above the most sensitive upper limit set at the signal frequency by the isolated searches listed in Section 5, regardless of the $\dot{f}$ range covered by that search. We count as detectable any binary signal whose amplitude lies above the most sensitive upper limit set at the signal frequency by any of the binary searches listed above, regardless of the $\dot{f}$ and orbital parameter ranges covered by that search. This is a reasonable assumption because the most sensitive isolated and binary searches, each in its own category, are very close in sensitivity to each other, regardless of their target $\dot{f}$ and orbital parameter ranges.

The sensitivity of third-generation detectors is estimated by rescaling the search sensitivity depth, as explained in the previous section. Differently than what was done in the case of normal neutron stars, however, for isolated objects we also consider the Falcon search because the $\dot{f}$ range surveyed by this search is compatible with that of recycled neutron stars.

We also consider a mixed population with 58% neutron stars in binaries and 42% isolated objects, based on the fraction of binary-to-isolated known MSPs. The results are shown in Figure 12 and are summarized in Table 7.

We find no currently detectable signals from neutron stars in binaries in 100 realizations of the population, and only one out of 100 realizations assuming all the population is composed of isolated neutron stars. With third-generation detectors, assuming a mixed population of isolated/binary recycled neutron stars, the average number of detectable signals varies approximately between 0.2 and 6, with the exact value depending on the relative fraction of the two populations. Assuming the same relative fraction as from the ATNF catalog results in an average number of detectable sources of ≈3. While in absolute terms, this is a lower number than for normal neutron stars, it represents a much higher fraction of the population. The fraction is higher by a factor of about 50.

7. Discussion

7.1. Novelty of Our Approach

The detectability of continuous gravitational waves depends on the frequency and amplitude of the signal. These quantities are in turn entangled with parameters of the source that are not independent of one another. For instance, the gravitational-wave amplitude depends on the ellipticity, spin frequency, and on the distance of the source. The frequency depends on the spin frequency at birth, on the age of the object, and on the parameters involved in the energy-braking mechanisms, e.g., the magnetic field and the ellipticity. The ellipticity may depend on the magnetic field. Distance and age are not completely independent quantities.

Several papers in the past two decades have studied the prospects for a detection of continuous gravitational waves by Galactic neutron stars (Palomba 2005; Knispel & Allen 2008; Wade et al. 2012; Lasky 2015; Woan et al. 2018; Cieślar et al. 2021; Soldateschi & Bucciantini 2021; Reed et al. 2021), but to the best of our knowledge, in no prior detectability analysis were all the effects mentioned above taken consistently into account together.

The first pioneering works of Palomba (2005) and Knispel & Allen (2008) only consider gravitars, i.e., neutron stars that are

loosing rotational energy solely due to gravitational radiation. The gravitar scenario simplifies calculations and is an intriguing one to explore, but it is not clear that a population like that exists.

Wade et al. (2012) are the first who take into account magnetized neutron stars, although they consider unphysical populations in which each neutron star has the same magnetic field and ellipticity values.

Cieślar et al. (2021) make a detectability assessment of a population of nonaxisymmetric neutron stars all born with the same ellipticity that decays exponentially with time. The distribution of sky positions and frequency is based on a single synthetic population that evolved neglecting the gravitational wave spin-down contribution.

Soldateschi & Bucciantini (2021) assess the detectability of continuous waves emitted by a synthetic population of Galactic neutron stars (both normal and recycled) whose deformation is caused by their magnetic field (Soldateschi et al. 2021). They do not model the spin evolution, but rather sample the spin frequency from the ATNF catalog and randomly assign magnetic fields. In doing so, the correlation between magnetic field and spin frequency is lost. This explains why they find currently detectable magnetically deformed sources that in their case indeed correspond to millisecond pulsars. Current observational results—no detections—differ from these predictions.

Reed et al. (2021) consider continuous gravitational-wave emission from a Galactic population of neutron stars, all equally deformed. They study the fraction of the Galactic population that is probed by different searches as a function of the assumed ellipticity value. Their results characterize the significance of the ellipticity constraints of observational results and can be used in turn to choose the target parameter space for future searches. The focus of their work is quite different from that investigated here.

In this paper, we produce a synthetic neutron star population, consistently evolved since birth in frequency and position, based on initial positions, kicks, spins, ellipticities, and magnetic field values. The age and position of each newly born neutron star is based on the remnant seeding it.

This is the first study that simulates the remnant population seeding the neutron stars. This is in principle important in order to model dependences of the remnant mass, position, and age on those of the newly born neutron star, such as the birth spin frequency, initial kick, and magnetic field. As we discuss in Section 7.3, in this first study, we made a number of simplifying assumptions. Nevertheless, we stress here the value of an ab initio framework because it allows us to naturally fold in more realistic models as they become available and to improve the reliability of the predictions.

Whereas previous studies have by and large adopted a single model, we consider two broad categories of models: agnostic (A) and empirical (E). The agnostic models use uninformed priors on the broadest possible physically motivated parameter range. The empirical models use more informative priors that are reasonably well accepted in the astrophysical community. From the different detectability profiles that stem from these different populations, we learn about the population parameters that mostly affect the detectability, about the range of detection probability, and about what we can learn from nondetections.

Finally, a number of studies (e.g., Cieślar et al. 2021; Soldateschi & Bucciantini 2021) adopt a detectability criterion

$(h_0^{\text{min.det.}} = 11.4 \sqrt{\dfrac{S_n}{T_{\text{obs}}}}$, where S_n is the detector noise and T_{obs} is the observation time) that does not apply to large surveys and overestimates the search sensitivity. We use a robust detection criterion, based on the measured sensitivity of broad surveys. The minimum detectable intrinsic strain amplitude is $h_0^{\text{min.det.}} = \dfrac{\sqrt{S_n}}{\mathcal{D}}$, where $\mathcal{D}$ is the sensitivity depth of the search (Behnke et al. 2015; Dreissigacker et al. 2018), and for the isolated neutron star surveys considered here, it is $\mathcal{D} \approx 55$ $[1/\sqrt{\text{Hz}}]$.

7.2. Results

We find that normal neutron stars that might be detectable in the foreseeable future must have an ellipticity that is not solely due to magnetic field deformations. In fact, whereas large magnetic fields can produce large deformations, they also cause the fast spin-down of the frequency to values that are too low for a signal to be detectable. For instance, a magnetic field of 10^{14} G can cause an ellipticity $\approx 10^{-6}$, but it yields a spin-down time of ≈ 10 yr, which makes these sources extremely rare and practically impossible to find within one kiloparsec of Earth (which is the reach of current detectors for that ellipticity).

To obtain sufficiently high ellipticities and at the same time avoid fast spin-downs, the poloidal magnetic field component should be much smaller than the toroidal component, i.e., the value of Λ should be very low (see Equation (3)). If we perform our simulations by progressively decreasing Λ, we find that in order to have a 10% chance of detection,[14] $\Lambda \lesssim 10^{-6}$. The stability of these strongly toroidal-dominated configurations is questioned in a number of studies (Lander & Jones 2009; Ciolfi et al. 2010; Lasky et al. 2012; Ciolfi & Rezzolla 2013; Lander et al. 2021).

Detectable objects with not purely magnetic deformations (A2 models) have ellipticity values greater than 10^{-7} and magnetic fields between $\approx 10^{10}$ and $\approx 10^{12}$ G. This is a rather narrow range of magnetic field and ellipticity values: at higher magnetic fields, the spin-down age decreases and causes objects that spin in-band increasingly rare. The ellipticity further down-selects on this sample based on the reach of the detectors at that ellipticity value. We provide an empirical expression for the expected number of objects for different intervals of B, ε in this range (Equation (14)).

It is not settled whether values of the ellipticity of $\approx 10^{-6}$, necessary for a detection at current sensitivities, are actually possible. Gittins et al. (2020) and Gittins & Andersson (2021) have proposed a new way to assess the maximally sustainable crustal strain in neutron stars. Their most optimistic results generally predict maximum ellipticities of about $\approx 5 \cdot 10^{-7}$ (see Table 1 of Gittins et al. 2020), which is more than an order of magnitude lower than the value adopted here at 10^{-5} for the highest ellipticity (see Equations (4) and (6)). If we set 5×10^{-7} as the maximum ellipticity of our synthetic neutron stars and set a log-uniform distribution down to a value determined by the magnetic field (namely Model 2 ellipticities), the outcomes of our simulations change dramatically: the bulk of the strongest signals generally lie about an order of magnitude below the current best upper limits, with only three currently detectable signals out of 100 realizations from model A2$_{\text{high}}$ and only two from model A2$_{\text{low}}$. This means a reduction in the total number of

---

[14] This estimate was obtained by maintaining $\varepsilon_{\max} = 10^{-5}$ as the maximum possible ellipticity.

currently detectable sources by a factor between 40 and 57. We point out, however, that Morales & Horowitz (2022) have recently shown that ellipticities this low are not a necessary consequence of the Gittins et al. (2020) approach.

The number of detectable sources increases by more than two orders of magnitude for searches on data from third-generation detectors. This result is in line with what was found by Reed et al. (2021). The increased low-frequency performance allows us to intercept a plentiful population of weak sources spinning below 20 Hz. If third-generation detectors do not detect a continuous gravitational signal, this excludes a maximum ellipticity at the 10^{-5} level, at least for the very broad A models.

Generally, magnetic field decay increases the chances of detection: for the third-generation detectors, we also find that sources drawn from the empirical model populations of Section 3.2 begin to become detectable, with model E2$_{unif}$ yielding the most optimistic predictions with an average of 5.2 detectable sources. Consistently with this, Cieślar et al.— whose model includes magnetic field decay—also find detectable signals, but overestimate the sources by a factor ≈ 5 because their spin evolution neglects the gravitational-wave spin-down, which instead contributes to pushing a significant number of sources out of the band (see Section 5.2.3).

Computational cost might be saved in all-sky surveys by restricting the searches to $\pm 15°$ of the Galactic plane and by limiting the frequency derivative range as a function of frequency, as discussed in Section 5.2.2—currently, the only scenarios that produce detectable signals favor the frequency range [60–550] Hz. To which extent these savings might be usefully reinvested, yielding a more sensitive search, needs to be evaluated in the context of an optimization scheme such as that designed for targeted searches (Ming et al. 2016, 2018). Our synthetic populations provide a key element for such studies.

Our simple recycled neutron star model predicts that an upcoming detection from these stars is very unlikely merely due to the much lower number of objects compared to normal neutron stars. However, the fraction of objects in-band is much higher, and this yields promising prospects for the detectability by third-generation detectors. We find that the expected number of detectable sources by third-generation detectors lies between 0.2 and 6, depending on the ratio of isolated neutron stars to neutron stars in binary systems. Assuming that the relative abundance of the two subpopulations is the same as the currently observed abundance in MSPs, the number of detectable sources is ≈ 3. We stress, however, that our analysis of recycled neutron stars constitutes an early-stage investigation and contains a number of simplifying assumptions that are discussed in the next section.

7.3. Caveats

7.3.1. Remnant Population

We assume a single exponential star formation history that is spatially invariant across the Galaxy. We neglect the lifespan of massive stars and assume the same fraction of the entire stellar mass to be neutron stars for progenitors older than about 4 Myr (i.e., the onset age for a stellar population to start producing neutron stars). This will overestimate the number of neutron stars that are younger than approximately 30 Myr. The impact on the detectability might be significant—it may be reducing

the detection probability even by a factor of 10—because most of the detectable objects are younger than 10^7 yr.

We assume a relatively wide mass range to obtain neutron star remnants. The upper mass limit may decrease if—for example—we assume initial rotational velocity in the progenitor.

7.3.2. Normal Neutron Star Population

Our modeling of the magnetic field decay is independent of the value of the field at birth. This might constitute an oversimplification—in fact. Gullón et al. (2014) find a correlation between the magnitude of the field at birth and the decay timescale, with larger fields decaying much faster than smaller ones. As shown in Figure 8, most of our future detectable sources in model E2 are born with $B \lesssim 10^{12}$G and at the present time have fields that are about four orders of magnitude smaller. It is not clear how a decay timescale dependent on the magnetic field at birth would impact our results. It may bring in-band highly magnetic field sources, whose field would decrease faster than in our models. Conversely, it may push sources with $B \lesssim 10^{12}$G out of the band, which in our models are detectable due to the slower decay.

7.3.3. Recycled Neutron Star Population

We have assumed a constant birthrate of one every 200,000 yr. The chosen value is important as it directly determines the total number of fast-spinning neutron stars, on which the number of detectable sources directly depends. Since the rebirth of a recycled neutron star is not followed by any recordable event, there are no direct measurements of the birthrate, and all predictions stem from population synthesis simulations and span three orders of magnitude. We follow Story et al. (2007) and consider 60,000 objects, but other studies predict as little as 10^3 stars (Pfahl et al. 2003) or as many as 10^6 (Zhu et al. 2015).

Our analysis of recycled neutron stars ignores accreting systems, which are very interesting as the accretion process may provide a natural source of asymmetry. It has in fact long been proposed that gravitational-wave emission could provide the torque-balancing mechanism that explains why no accreting neutron star is spinning anywhere close to the maximum possible spin rate (Wagoner 1984; Patruno et al. 2017). In this case, it can be argued that the gravitational-wave amplitude grows with the mass accretion rate, and hence with the luminosity from the accretion process. This is what makes very bright accreting objects such as Sco X-1 particularly interesting (Zhang et al. 2021). On the other hand, bright objects are easier to observe in the EM domain, and one could argue that the determination of their properties should more usefully rely on EM observations and that the case for population studies such as this is less compelling for these systems.

7.4. Prospects and Conclusions

We have presented results from a broad ab initio study of the detectability of continuous gravitational waves emitted by fast-rotating neutron stars. This is the first study of this type.

Our predictions are consistent with the null-detection results of the latest all-sky searches. A detection is currently not excluded, but it is limited to stars with deformations that are not just due to the magnetic field (A2 models), and even in this

case, it is far from guaranteed (Table 3). In fact, the low number of detectable sources means that a change of a factor of two in the size of the progenitor population, for instance—which could very easily come about—could produce significant changes in the chances of observing the first signal. With detectors just a factor of two more sensitive, the situation changes substantially, making the prospects of detection rather more robust, at least for our agnostic models (Table 4).

One way to increase the sensitivity is to limit the searched parameter space. Our results indicate that at the present time, the detection probability would not be significantly impacted by restricting the search to $\pm 15°$ of the Galactic plane and by limiting the frequency range below 600 Hz. We stress again that with low numbers of expected detectable sources, decisions to limit the search space must be carefully evaluated against the sensitivity gains that these savings produce.

The main two enhancement that we foresee concern the remnant population and the modeling of the recycled neutron star population:

1. In future work, we plan to trace the formation of neutron stars in young stellar progenitor populations and to consider different star formation histories within our Galaxy, enlightened by recent massive stellar spectroscopic surveys (Lian et al. 2020a, 2020b, 2018; Spitoni et al. 2021).
2. The outcome of the recycling is intimately coupled with the binary parameters, which we have ignored. To consider the recycling process is a project of its own, but we see in it great potential in providing guidance on how to best search the orbital parameter space.

Thanks to the upcoming pulsar surveys, the number of known neutron stars is expected to grow in the course of this decade to over 20,000 (Smits et al. 2009). While this will probably not significantly advance our understanding of the degree of deformation of neutron stars, it will shed light on the evolution of neutron stars and on their parameters, such as their spin and spatial distributions, age, and magnetic field. Feeding into studies such as the one presented here, this information will allow us to make more reliable predictions of the parameters of detectable continuous gravitational waves, and it will guide the observational surveys. When signals are detected, these studies will enable inferences on the properties of the underlying population—including properties to which electromagnetic observations are completely blind.

Acknowledgments

Appendix A
Numerical Integration

A.1. A Models

In the A models, the magnetic fields are independent of time. Equation (1) can be analytically integrated, and we obtain Equation (16). Unfortunately, the latter equation cannot be inverted to give $\nu(t)$. We follow Wade et al. and find the frequency at the present time as one of the zeros of Equation (16), consistent with a monotonic spin-down. We do this by using the root-finding method `brentq` from the `scipy` library.

A.2. E Models

For these models, the magnetic fields have the time dependence defined in Equation (8), and it is not possible to analytically integrate Equation (1).

We proceed as follows. Unlike the time-independent magnetic field case, γ, defined in Equation (11), is a monotonically increasing function of time through $B(t)$. If Equation (11) is satisfied at the birth time but not at the present time, then it means that there exists a time t^* such that

$$\gamma(t^*) = 10^{-8} \text{ s}^2. \tag{A1}$$

We recall that our condition for pure magnetic dipole emission is Equation (11), $\gamma < 10^{-8} \text{ s}^2$. So Equation (A1) tells us that the condition for pure magneto-dipole spin-down is satisfied until t^*, and for $t > t^*$, the magnetic field is so small that we can no longer ignore the gravitational-wave spin-down contribution. We thus integrate analytically, approximating the spin-down to be purely magneto-dipolar until t^*, and then integrate numerically up to the present time. If Equation (11) is not valid at birth, we integrate numerically for the entire age of the object. We use the `odeint` function of the `scipy` library, limiting the maximum number of steps per integration to 10,000.

Appendix B
Intrinsic Detection Odds as a Function of Birth Spin Frequency

Starting from the results of our synthetic population, we wish to compare the intrinsic chances of a detection for sources whose birth spin frequency belongs to the two different bands, $\mathcal{B}_1 = [2, 300]$ Hz and $\mathcal{B}_2 = [300, 1200]$ Hz, i.e., factoring out the fact that the two bands have a different size. We consider the results from model A2$_{\text{high}}$.

In the 100 realizations we performed, we find 362 currently detectable sources. Of these, 124 ($\approx$34% of 362) have a birth spin frequency $\nu_0 \in \mathcal{B}_1$, while the remaining 238 ($\approx$66% of 362) have $\nu_0 \in \mathcal{B}_2$. In the A2$_{\text{high}}$ model, birth spin frequencies are distributed log-uniformly between 2 and 1200 Hz, which means that $\approx$78% of the neutron star population is born with $\nu_0 \in \mathcal{B}_1$ and the remaining $\approx$22% with $\nu_0 \in \mathcal{B}_2$ (the two bands have indeed different sizes). If N^{TOT} is the total number of sources in the 100 realizations we performed, there are $\approx 0.78 \cdot N^{\text{TOT}}$ sources born with $\nu_0 \in \mathcal{B}_1$ and $\approx 0.22 \cdot N^{\text{TOT}}$ born with $\nu_0 \in \mathcal{B}_2$. The two fractions

$$\mathcal{F}_{\mathcal{B}_1}^{\text{det}} = \frac{124}{0.78 \cdot N^{\text{TOT}}} \text{ and } \mathcal{F}_{\mathcal{B}_2}^{\text{det}} = \frac{238}{0.22 \cdot N^{\text{TOT}}} \tag{B1}$$

represent the chances that a source be detectable if it was born with $\nu_0 \in \mathcal{B}_1$ and $\nu_0 \in \mathcal{B}_2$, respectively, regardless of the size of the two bands. In practice, for every source born with $\nu_0 \in \mathcal{B}_1$ ($\nu_0 \in \mathcal{B}_2$), a fraction $\mathcal{F}_{\mathcal{B}_1}^{\text{det}}$ ($\mathcal{F}_{\mathcal{B}_2}^{\text{det}}$) is detectable. Finally, the ratio

$$\Lambda = \frac{\mathcal{F}_{\mathcal{B}_2}^{\text{det}}}{\mathcal{F}_{\mathcal{B}_1}^{\text{det}}} \tag{B2}$$

gives the intrinsic detection odds for a signal from a source born with $\nu_0 \in \mathcal{B}_2$ against those from a source born with $\nu_0 \in \mathcal{B}_1$. Plugging Equation (B1) in Equaiton (B2), we obtain $\Lambda \approx 6.8$.

ORCID iDs

Gianluca Pagliaro ⬤ https://orcid.org/0009-0008-1886-8912
Maria Alessandra Papa ⬤ https://orcid.org/0000-0002-1007-5298
Jing Ming ⬤ https://orcid.org/0000-0002-2150-3235
Jianhui Lian ⬤ https://orcid.org/0000-0001-5258-1466
Daichi Tsuna ⬤ https://orcid.org/0000-0002-6347-3089
Claudia Maraston ⬤ https://orcid.org/0000-0001-7711-3677
Daniel Thomas ⬤ https://orcid.org/0000-0002-6325-5671

References

Abbott, R., Abbott, T. D., Abraham, S., et al. 2021a, PhRvD, 103, 064017
Abbott, R., Abbott, T. D., Abraham, S., et al. 2021b, ApJ, 921, 80
Abbott, R., Abbott, T. D., Abraham, S., et al. 2021c, PhRvD, 104, 082004
Abbott, R., Abbott, T. D., Acernese, F., et al. 2022b, ApJ, 932, 133
Abbott, R., Abbott, T. D., Acernese, F., et al. 2022c, PhRvD, 105, 022002
Abbott, R., Abe, H., Acernese, F., et al. 2022a, ApJ, 935, 1
Abbott, R., Abe, H., Acernese, F., et al. 2022d, PhRvD, 106, 062002
Abbott, R., Abe, H., Acernese, F., et al. 2022e, PhRvD, 106, 102008
Akgün, T., Reisenegger, A., Mastrano, A., & Marchant, P. 2013, MNRAS, 433, 2445
Alpar, M. A., Cheng, A. F., Ruderman, M. A., & Shaham, J. 1982, Natur, 300, 728
Andersson, N. 2020, Gravitational-wave Astronomy: Exploring the Dark Side of the Universe (Oxford: Oxford Univ. Press), 333
Ashok, A., Beheshtipour, B., Papa, M. A., et al. 2021, ApJ, 923, 85
Behnke, B., Papa, M. A., & Prix, R. 2015, PhRvD, 91, 064007
Bhattacharya, D., & van den Heuvel, E. P. J. 1991, PhR, 203, 1
Bildsten, L. 1998, ApJL, 501, L89
Bland-Hawthorn, J., & Gerhard, O. 2016, ARA&A, 54, 529
Bonazzola, S., & Gourgoulhon, E. 1996, A&A, 312, 675
Bovy, J. 2017, MNRAS, 470, 1360
Braithwaite, J. 2007, A&A, 469, 275
Braithwaite, J. 2009, MNRAS, 397, 763
Brown, E. F., & Bildsten, L. 1998, ApJ, 496, 915
Camelio, G., Gualtieri, L., Pons, J. A., & Ferrari, V. 2016, PhRvD, 94, 024008
Chakrabarty, D. 2008, in AIP Conf. Proc. 1068, A Decade of Accreting Millisecond X-Ray Pulsars, ed. R. Wijnands et al. (Melville, NY: AIP), 67
Chandrasekhar, S., & Fermi, E. 1953, ApJ, 118, 116
Chattopadhyay, D., Stevenson, S., Hurley, J. R., Rossi, L. J., & Flynn, C. 2020, MNRAS, 494, 1587
Chiappini, C., Matteucci, F., & Romano, D. 2001, ApJ, 554, 1044
Cieślar, M., Bulik, T., Curyło, M., et al. 2021, A&A, 649, A92
Cieślar, M., Bulik, T., Osłowski, S., et al. 2020, MNRAS, 492, 4043
Ciolfi, R., Ferrari, V., & Gualtieri, L. 2010, MNRAS, 406, 2540
Ciolfi, R., Lander, S. K., Manca, G. M., & Rezzolla, L. 2011, ApJL, 736, L6
Ciolfi, R., & Rezzolla, L. 2013, MNRAS, 435, L43
Covas, P., & Sintes, A. M. 2020, PhRvL, 124, 191102
Covas, P. B., Papa, M. A., Prix, R., & Owen, B. J. 2022, ApJL, 929, L19
Cutler, C., & Jones, D. I. 2000, PhRvD, 63, 024002
Dergachev, V., & Papa, M. A. 2020, PhRvL, 125, 171101
Dergachev, V., & Papa, M. A. 2021, PhRvD, 104, 043003
Dergachev, V., & Papa, M. A. 2023, PhRvX, 13, 021020
Diehl, R., et al. 2006, Natur, 439, 45
Dreissigacker, C., Prix, R., & Wette, K. 2018, PhRvD, 98, 084058
Dwyer, S., Sigg, D., Ballmer, S. W., et al. 2015, PhRvD, 91, 082001
Enoto, T., Kisaka, S., & Shibata, S. 2019, RPPh, 82, 106901
Faucher-Giguère, C.-A., & Kaspi, V. M. 2006, ApJ, 643, 332
Ferrario, L., & Wickramasinghe, D. 2007, MNRAS, 375, 1009
Ferraro, V. C. A. 1954, ApJ, 119, 407
Flynn, C., Holmberg, J., Portinari, L., Fuchs, B., & Jahreiß, H. 2006, MNRAS, 372, 1149
Giliberti, E., & Cambiotti, G. 2022, MNRAS, 511, 3365
Gittins, F., & Andersson, N. 2021, MNRAS, 507, 116
Gittins, F., Andersson, N., & Jones, D. I. 2020, MNRAS, 500, 5570
Gonthier, P. L., Guilder, R. V., & Harding, A. K. 2004, ApJ, 604, 775
Grégoire, T., & Knödlseder, J. 2013, A&A, 554, A62
Gullón, M., Miralles, J. A., Viganò, D., & Pons, J. A. 2014, MNRAS, 443, 1891
Gullón, M., Pons, J. A., Miralles, J. A., et al. 2015, MNRAS, 454, 615
Haskell, B. 2008, CQGra, 25, 114049
Haskell, B., Jones, D. I., & Andersson, N. 2006, MNRAS, 373, 1423

Haskell, B., Samuelsson, L., Glampedakis, K., & Andersson, N. 2008, MNRAS, 385, 531
Haskell, B., Zdunik, J. L., Fortin, M., et al. 2018, A&A, 620, A69
Heger, A., Langer, N., & Woosley, S. E. 2000, ApJ, 528, 368
Heger, A., Woosley, S. E., Langer, N., & Spruit, H. C. 2004, in Symp. IAU, 215, 591
Heger, A., Woosley, S. E., & Spruit, H. C. 2005, ApJ, 626, 350
Hild, S., Abernathy, M., Acernese, F., et al. 2011, CQGra, 28, 094013
Horowitz, C. J., & Kadau, K. 2009, PhRvL, 102, 191102
Janka, H.-T., Kifonidis, K., & Rampp, M. 2001, in Physics of Neutron Star Interiors (Lecture Notes in Physics) Vol. 578, ed. D. Blaschke, N. K. Glendenning, & A. Sedrakian (Berlin: Springer), 363
Kaspi, V. M., & Kramer, M. 2016, arXiv:1602.07738
Katz, J. I. 1989, MNRAS, 239, 751
Kennicutt, R. C. J. 1998, ApJ, 498, 541
Kiuchi, K., Shibata, M., & Yoshida, S. 2008, PhRvD, 78, 024029
Knispel, B., & Allen, B. 2008, PhRvD, 78, 044031
Kroupa, P. 2001, MNRAS, 322, 231
Lander, S. K., Haensel, P., Haskell, B., Zdunik, J. L., & Fortin, M. 2021, MNRAS, 503, 875
Lander, S. K., & Jones, D. I. 2009, MNRAS, 395, 2162
Lander, S. K., & Jones, D. I. 2011, MNRAS, 412, 1730
Lasky, P. D. 2015, PASA, 32, e034
Lasky, P. D., Zink, B., & Kokkotas, K. D. 2012, arXiv:1203.3590
Leung, H. W., & Bovy, J. 2019, MNRAS, 489, 2079
Lian, J., Thomas, D., Maraston, C., et al. 2018, MNRAS, 474, 1143
Lian, J., Thomas, D., Maraston, C., et al. 2020a, MNRAS, 494, 2561
Lian, J., Thomas, D., Maraston, C., et al. 2020b, MNRAS, 497, 2371
Licquia, T. C., Newman, J. A., & Bershady, M. A. 2016, ApJ, 833, 220
Lorimer, D. R. 2008, LRR, 11, 8
Ma, L., & Fuller, J. 2019, MNRAS, 488, 4338
Mackereth, J. T., & Bovy, J. 2018, PASP, 130, 114501
Maggiore, M., Van Den Broeck, C., Bartolo, N., et al. 2020, JCAP, 2020, 050
Majewski, S. R., Schiavon, R. P., Frinchaboy, P. M., et al. 2017, AJ, 154, 94
Manchester, R. N., Hobbs, G. B., Teoh, A., & Hobbs, M. 2005, AJ, 129, 1993
Maraston, C. 1998, MNRAS, 300, 872
Maraston, C. 2005, MNRAS, 362, 799
Markey, P., & Tayler, R. J. 1973, MNRAS, 163, 77
Mastrano, A., Melatos, A., Reisenegger, A., & Akgün, T. 2011, MNRAS, 417, 2288
McKee, C. F., Parravano, A., & Hollenbach, D. J. 2015, ApJ, 814, 13
Melatos, A., & Payne, D. J. B. 2005, ApJ, 623, 1044
Ming, J., Krishnan, B., Papa, M. A., Aulbert, C., & Fehrmann, H. 2016, PhRvD, 93, 064011
Ming, J., Papa, M. A., Eggenstein, H.-B., et al. 2022, ApJ, 925, 8
Ming, J., Papa, M. A., Krishnan, B., et al. 2018, PhRvD, 97, 024051
Morales, J. A., & Horowitz, C. J. 2022, MNRAS, 517, 5610
Nieder, L., Clark, C. J., Kandel, D., et al. 2020, ApJL, 902, L46
Ostriker, J. P., & Gunn, J. E. 1969, ApJ, 157, 1395
Ott, C. D., Burrows, A., Thompson, T. A., Livne, E., & Walder, R. 2006, ApJS, 164, 130
Owen, B. J. 2005, PhRvL, 95, 211101
Owen, B. J., Lindblom, L., & Pinheiro, L. S. 2022, ApJL, 935, L7
Palomba, C. 2005, MNRAS, 359, 1150
Patruno, A., Haskell, B., & Andersson, N. 2017, ApJ, 850, 106
Perna, R., Soria, R., Pooley, D., & Stella, L. 2008, MNRAS, 384, 1638
Pfahl, E., Rappaport, S., & Podsiadlowski, P. 2003, ApJ, 597, 1036
Popov, S. B., Pons, J. A., Miralles, J. A., Boldin, P. A., & Posselt, B. 2010, MNRAS, 401, 2675
Popov, S. B., & Turolla, R. 2012, Ap&SS, 341, 457
Priymak, M., Melatos, A., & Payne, D. J. B. 2011, MNRAS, 417, 2696
Punturo, M., Abernathy, M., Acernese, F., et al. 2010, CQGra, 27, 194002
Radhakrishnan, V., & Srinivasan, G. 1982, CSci, 51, 1096
Rajbhandari, B., Owen, B. J., Caride, S., & Inta, R. 2021, PhRvD, 104, 122008
Reed, B. T., Deibel, A., & Horowitz, C. J. 2021, ApJ, 921, 89
Renzini, A., & Ciotti, L. 1993, ApJL, 416, L49
Renzini, A., Ciotti, L., D'Ercole, A., & Pellegrini, S. 1993, ApJ, 419, 52
Sartore, N., Ripamonti, E., Treves, A., & Turolla, R. 2010, A&A, 510, A23
Singh, A., & Papa, M. A. 2023, ApJ, 943, 99
Smits, R., Kramer, M., Stappers, B., et al. 2009, A&A, 493, 1161
Soldateschi, J., & Bucciantini, N. 2021, Galax, 9, 101
Soldateschi, J., Bucciantini, N., & Del Zanna, L. 2021, A&A, 654, A162
Spitoni, E., Verma, K., Silva Aguirre, V., et al. 2021, A&A, 647, A73
Srivastava, V., Davis, D., Kuns, K., et al. 2022, ApJ, 931, 22
Steltner, B., Papa, M. A., Eggenstein, H. B., et al. 2023, ApJ, 952, 55
Story, S. A., Gonthier, P. L., & Harding, A. K. 2007, ApJ, 671, 713

Tauris, T. M. 2011, in ASP Conf. Ser. 447, Evolution of Compact Binaries, ed. L. Schmidtobreick, M. R. Schreiber, & C. Tappert (San Francisco, CA: ASP), 285

Tayler, R. J. 1973, MNRAS, 161, 365

Tsuna, D., Kawanaka, N., & Totani, T. 2018, MNRAS, 477, 791

Ushomirsky, G., Cutler, C., & Bildsten, L. 2000, MNRAS, 319, 902

Viganò, D., Rea, N., Pons, J. A., et al. 2013, MNRAS, 434, 123

Vigelius, M., & Melatos, A. 2009, MNRAS, 395, 1972

Vigna-Gómez, A., Neijssel, C. J., Stevenson, S., et al. 2018, MNRAS, 481, 4009

Wade, L., Siemens, X., Kaplan, D. L., Knispel, B., & Allen, B. 2012, PhRvD, 86, 124011

Wagoner, R. V. 1984, ApJ, 278, 345

Woan, G., Pitkin, M. D., Haskell, B., Jones, D. I., & Lasky, P. D. 2018, ApJL, 863, L40

Wright, G. A. E. 1973, MNRAS, 162, 339

Zhang, Y., Papa, M. A., Krishnan, B., & Watts, A. L. 2021, ApJL, 906, L14

Zhu, C., Lü, G., & Wang, Z. 2015, MNRAS, 454, 1725